Nano Research

Open Access

Research Article

Tunable built-in electric field of homologous heterojunction regulated by nitrogen doped carbon to enhance water splitting

Daorui Wang[1,2], Shuo Wang[1], Haonan Zhang[1], Chenmeng Cui[1], Shijie Hao[2], Ping Qiu[2], Lirong Zheng[3] ✉, and Ying Yang[1] ✉

[1] College of Chemical Engineering and Environment, China University of Petroleum, Beijing 102249, China
[2] College of New Energy and Materials, China University of Petroleum, Beijing 102249, China
[3] Institute of High Energy Physics, Chinese Academy of Sciences, Beijing 100049, China

Cite this article: *Nano Research*, **2025**, *18*, 94907381. https://doi.org/10.26599/NR.2025.94907381

ABSTRACT: Engineering efficient bifunctional catalysts for hydrogen production is crucial for advancing hydrogenation technologies and reducing infrastructure costs. However, the inferior kinetics of water dissociation during the hydrogen evolution reaction (HER) and the sluggish OH^- adsorption during oxygen evolution reaction (OER) under alkaline conditions greatly hinder their electrolytic efficiencies. Given this, we established Ni_3S_2-MoS_2 heterojunctions with a tunable built-in electric field (BEF) by integrating nitrogen-doped carbon (NC) to enhance water splitting. Specifically, NC-coupled Ni_3S_2-MoS_2 heterojunctions were synthesized by assembling chitosan, thiourea, and sodium molybdate onto nickel foam, followed by carbonization. The chitosan amount was adjusted to control the NC content, which in turn modulated the BEF of the Ni_3S_2-MoS_2 heterojunctions. Profiting from the strong electronegativity, N element serves as an electron acceptor, and the BEF of Ni_3S_2-MoS_2 is effectively manipulated by NC, facilitating fast electron transfer and targeted modulation of active sites. Consequently, the optimized NC-coupled Ni_3S_2-MoS_2 heterojunction with the robust BEF exhibits competitive overpotentials of 75 and 146 mV at 10 mA·cm^{-2} for HER and OER, respectively. Relative to Ni_3S_2-MoS_2, theoretical calculations confirm that the robust BEF of NC-coupled Ni_3S_2-MoS_2 lowers the water dissociation energy by 0.62 eV and increases the OH^- adsorption energy by 0.22 eV for HER and OER, respectively. Moreover, the robust BEF of NC-coupled Ni_3S_2-MoS_2 contributes to reconstructing a highly active NiOOH phase. This pioneering study introduces a groundbreaking BEF architecture to effectively modulate the surface/interface charge states of electrocatalysts, opening new avenues for exploring robust homologous heterostructures in the future.

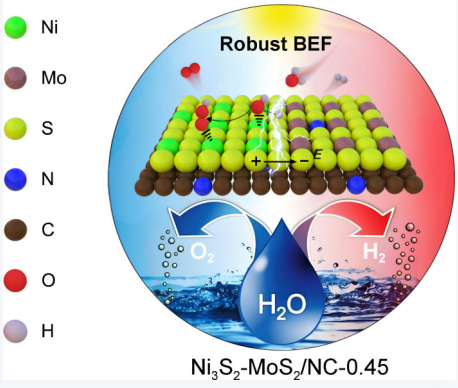

Ni_3S_2-MoS_2/NC-0.45

KEYWORDS: built-in electric field, water splitting, homologous heterostructures, nitrogen doped carbon, charge states

1 Introduction

Alkaline electrocatalytic hydrogen production has garnered significant attention owing to its cost-effectiveness and environmental sustainability, positioning it as a critical pathway for alleviating the fossil energy crisis and curbing greenhouse gas emissions [1–3]. In the backdrop of alkaline water electrolysis, the hydrogen evolution reaction (HER) at the cathode and the oxygen evolution reaction (OER) at the anode stand as critical electrochemical processes. However, the large energy barrier for water dissociation results in inadequate hydrogen coverage during HER, exerting the rate-limiting step for HER [4–7]. Simultaneously, the high adsorption energy barrier for OH^- in the initial stages of OER for most catalysts gives rise to sluggish reaction kinetics [8–10]. This not only increases the input voltage for the overall water splitting (OWS) process but also diminishes the catalyst's activity and the energy conversion efficiency of the entire apparatus. To address these challenges, developing novel, efficient bifunctional catalysts has emerged as a research hotspot. By employing judicious structural design to govern the adsorption behavior of catalytic active sites, the configurations not only enhance energy conversion efficiency and reduce equipment costs but also hold profound implications for realizing a clean, sustainable energy supply.

Given this, pioneering research has concentrated on constructing

Received: February 1, 2025; **Revised:** March 15, 2025
Accepted: March 17, 2025

✉Address correspondence to Ying Yang, yyang@cup.edu.cn; Lirong Zheng, zhenglr@ihep.ac.cn

heterojunctions to improve electron transfer across interfaces, and the space charge effect could optimize the adsorption of targeted ions to tackle these challenges. Some research focuses on exploring combinations of metal hydroxides and transition metal compounds within heterojunctions, where the oxygen-affine metal hydroxide sites interact with oxygen in water molecules via hydrogen bonding, thereby facilitating water dissociation during HER. Beyond that, electron-deficient metal sulfides enhance OH^- adsorption through electrostatic interactions [11–13]. However, metal hydroxides with low electrical conductivity hinder electron transfer, and mismatched lattices at interface atoms restrict their capacity for water dissociation and OH^- adsorption. Subsequently, research has focused on developing homologous heterojunctions composed of transition metal compounds, where nucleophilic components promote OH^- adsorption, and electrophilic components facilitate water dissociation [14–17]. Despite these advancements, heterojunctions composed of elements with similar electronegativities can lead to saturated interface electric fields, which impede further improvements in electron transfer capabilities. Moreover, active species are susceptible to corrosion by strong alkaline solutions, leading to the loss of active sites and ineffective regulation of electroactive sites. As a result, the output voltage of water splitting remains over 1.5 V at 10 $mA{\cdot}cm^{-2}$ for these catalysts. Therefore, it is imperative to develop heterojunction interfaces that possess high stability and robust built-in electric field (BEF) to propel the advancement of electrocatalysis in water electrolysis [18].

In response to the aforementioned challenges, incorporating nitrogen-doped carbon (NC) into heterojunctions is a promising approach for modulating the BEF. N atom with high electronegativity serves as an electron acceptor, which could tailor the band structure within the active phases of the heterojunction, thereby optimizing the adsorption/desorption behavior of active sites at the interface. Moreover, the carbon layer could protect the heterointerface from corrosion by alkaline solution to form a stable BEF [19, 20]. This dual-functionality design could effectively enhance the utilization efficiency of the active sites. Therefore, the strong Coulombic forces effectively facilitate the cleavage of H–OH bonds in polar water molecules under the influence of a robust BEF, thereby boosting the water dissociation during HER [21, 22]. Simultaneously, the strong BEF could induce a higher number of electron transfers at the active sites, contributing to the formation of high-valence metal species and enhancing hydroxide adsorption [23]. Such superiorities may reduce the energy barrier for the formation of OOH* intermediates and promote the reconstruction of highly active phases. However, regarding the modulation of the BEF, conventional methods typically involve the introduction of vacancy structures [24, 25]. Yet, these metastable vacancy-type heterojunctions are susceptible to deactivation during OER [26]. Alternatively, screening the components with different work functions to create robust BEF can compromise their controllability [27, 28], which may introduce unexpected structural changes such as chemical bond breakage. Comprehensive research has struggled to tailor the BEF effectively, complicating the determination of whether the observed performance improvements arise from synergistic effects of individual components or the BEF influence. Moreover, the BEF in heterojunction tends to diminish under harsh oxidation environments. Therefore, constructing the robust BEF is crucial for revealing its structure–activity relationship and remains an urgent challenge that demands immediate attention.

Herein, we have successfully modulated the BEF of Ni_3S_2-MoS_2 on nickel foam (NF) by integrating NC through a hydrothermal and pyrolysis strategy. The BEF intensity between Ni_3S_2 and MoS_2 allows for efficient regulation by optimizing the coordination between NC and MoS_2 component in the Ni_3S_2-MoS_2 heterojunction. This optimization was achieved by adjusting the chitosan concentration under the electrostatic interactions between amino groups of chitosan and molybdate ions during hydrothermal and carbonization processes. As expected, the resultant nitrogen-doped Ni_3S_2-MoS_2 heterostructure, endowed with a robust BEF, demonstrates remarkable electrocatalytic performance with overpotentials of merely 75 and 146 mV at a current density of 10 $mA{\cdot}cm^{-2}$ for the HER and OER, respectively. Therefore, this versatile catalyst provides a stable output voltage of 1.46 V under overall water splitting conditions at 10 $mA{\cdot}cm^{-2}$ and maintains prolonged electrolysis performance at 0.2 $A{\cdot}cm^{-2}$ for an extended 100 h period. Such endurance surpasses that of most homologous heterojunctions currently known. Theoretical calculations further reveal that the strong BEF of the NC optimized Ni_3S_2-MoS_2 heterostructure electrode is identified as the driving force that facilitates water dissociation for the HER and enhances OH^- adsorption and rapid surface reconstruction for OER. Moreover, the NC substrate effectively prevents the loss of active components, thereby contributing to a stable BEF for upgrading the electrocatalytic activity.

2 Experimental

2.1 Chemicals

Sodium molybdate (Na_2MoO_4, 99%), thiourea (CH_4N_2S, 99%), and acetic acid ($C_2H_4O_2$, 36%) were sourced from Macklin. Chitosan (CS, 95% deacetylation degree) and the triblock copolymer $EO_{20}PO_{70}EO_{20}$ (P123, M_W = 5800) were procured from Sigma Aladdin. Hydrochloric acid (HCl, 37%), phosphate-buffered saline (PBS), and potassium hydroxide (KOH, 85%) were obtained from Beijing Chemical Company. Nickel foam (99%) was supplied by Kunshan Shangte New Material Co., Ltd. All reagents used in the experiments were employed as received, without any further purification processes.

2.2 Synthesis of Ni_3S_2-MoS_2/NC

A piece of NF (2 cm × 3 cm) was initially treated by ultrasonic cleaning in a 3 M HCl solution, followed by thorough rinsing with deionized water to remove any surface impurities. A specific quantity of CS (0.15, 0.30, 0.45, and 0.60 g) and 0.4 g Pluronic P123 were then dissolved in 60 mL of deionized water containing 0.9 g acetic acid. This solution was stirred for 1 h to achieve a homogenous mixture. Following this, 0.5 mmol Na_2MoO_4 and 4 mol CH_4N_2S were gradually introduced into the chitosan solution, with stirring continuing for another hour to facilitate the formation of precursor complexes. The cleaned NF was immersed in the precursor mixture and then processed under hydrothermal conditions at a temperature of 220 °C for a duration of 24 h, yielding a Ni_3S_2-MoS_2 and CS composite on the NF substrate. Finally, the synthesized Ni_3S_2-MoS_2/CS composite was subjected to carbonization under a N_2 atmosphere at 650 °C for 1 h at 5 $°C{\cdot}min^{-1}$. The final carbonized product was designated as Ni_3S_2-MoS_2/NC-*X*, where *X* refers to the feeding weight of CS. The mass loading of Ni_3S_2-MoS_2/NC-*X* catalysts was determined to be 3 $mg{\cdot}cm^{-2}$ based on the mass increase of the bare Ni foam.

For comparison, the method for preparing Ni_3S_2-MoS_2 on NF is similar to that of Ni_3S_2-MoS_2/NC-*X*, but without adding CS and acetic acid. Similarly, Ni_3S_2 catalyst was built on NF via hydrothermal treatment by adding 4 mmol CH_4N_2S into 60 mL deionized water and heating at 220 °C for 24 h. The MoS_2 powder was fabricated by previously reported method [29], which was then drop-cast on NF with a mass loading of 3 mg·cm^{-2}.

2.3 Material characterization

Crystalline structures were investigated via X-ray diffraction (XRD) using a Bruker D8 Advance device by employing a method of continuous scanning with Cu Kα radiation. The morphological aspects and elemental dispersion across the samples were scrutinized using a JEOL JEM-2100F transmission electron microscope. Raman spectroscopy was conducted with a HORIBA Scientific T6400 confocal Raman microscope. For a detailed examination of the surface chemical composition, X-ray photoelectron spectroscopy (XPS) was performed on an ESCALAB 250 system, calibrating all binding energies against the C 1s peak at 284.8 eV. The content of elements was determined by inductively coupled plasma spectrometry (ICP, Agilent ICPOES730). The Kelvin probe force microscopy (KPFM) images were recorded using atomic force microscopy (AFM, Bruker Icon). The surface potential was examined by a zeta potential analyzer (Malvern Zetasizer Nano ZS90). X-ray absorption fine structure (XAFS) spectra were obtained at the 1W1B station of the Beijing Synchrotron Radiation Facility, which were collected in transmission mode with the storage rings energy and beam current at 2.5 GeV and 250 mA, respectively. The entire set of spectra were gathered under ambient conditions. The obtained data were processed using the Athena software suite, which involved several steps including background removal, post-edge normalization, and X-ray absorption near edge structure (XANES) analysis.

2.4 Electrochemical test

Data from electrochemical experiments were obtained using a three/two-electrode setup connected to a CHI 760E workstation, which was manufactured in Shanghai, China. In the standard procedure, the catalyst that had been synthesized on the NF was directly utilized as the working electrode, alongside a Hg/HgO reference electrode and a graphite counter electrode. To ensure potential measurements were accurate, all the potentials were corrected for *iR* losses and further converted to the reversible hydrogen electrode (RHE) according to the Nernst equation. Besides, the solution was purged with N_2 for at least 0.5 h before each experiment to remove any dissolved oxygen from electrolyte. Cyclic voltammetry (CV) was performed for several cycles until a stable CV curve was recorded, fully activating the test conditions. For the assessment of catalytic activity, linear sweep voltammetry (LSV) was carried out at a scanning rate set to 5 mV·s^{-1}. The stability of the catalysts was evaluated using a constant current density method by employing the chronopotentiometry (CP) technique. The *ex situ* Raman test of OER was conducted at different potentials for 1 h to ensure surface reconstruction, and then the Ni_3S_2-MoS_2/NC-0.45 and Ni_3S_2-MoS_2 electrodes were immediately extracted from the electrolyte for Raman testing. The electrochemical active surface area (ECSA) was calculated from CV scans taken in the non-Faradaic region, with varying scan rates measured during reaction for HER and OER. Additionally, electrochemical impedance spectroscopy (EIS) was conducted to probe the impedance characteristics, with measurements taken over a frequency range from 10^5 to 0.01 Hz, using a small amplitude within 10 mV. Specific potentials of 1.53 V for OER and −0.1 V for HER were selected for EIS measurements. For the evaluation of water splitting, LSV curves were collected using a two-electrode configuration. The turnover frequency (TOF) for HER and OER was determined using the equations [30]

$$N = Q/2F \tag{1}$$

$$\mathrm{TOF} = J/mFN \tag{2}$$

In Eqs. (1) and (2), N corresponds to the mole number of the active sites; Q denotes the total charge passing during the electrochemical reaction; m signifies the mass of the catalyst used; J is the current density obtained from CV measurements at a scanning rate of 50 mV·s^{-1} in PBS solution. The symbol F represents the Faraday constant, which is a fundamental constant of electrochemistry.

2.5 Density functional theory (DFT) calculation

Spin-polarized DFT calculations were performed within the Vienna *ab initio* simulation package [31], using the projector augmented wave method, the generalized gradient approximation of Perdew–Burke–Ernzerhof functional [32], and the plane-wave basis set with an energy cutoff of 450 eV. The Brillouin zones were sampled by a gamma-centered 2 × 2 × 1 k-point mesh, while the vacuum region was set to be 12 Å along the *z*-axis to eliminate the interactions between neighboring models. The convergence criteria of structure optimization were set to be 10^{-5} eV for the electronic energy and 0.02 eV·Å^{-1} for the forces on each atom. The Ni_3S_2 (021)/MoS_2 (002) slab was constructed to explore the HER and OER activity of the Ni_3S_2-MoS_2, whereas N replaced S in the MoS_2 (002) slab to construe Ni_3S_2/N-MoS_2 model. For all slab models, the vacuum space was set to be over 15 Å. The DFT-D3 method was selected for the van der Waals correction [33]. The minimum energy paths and transition states were determined by the climbing image nudged elastic band method [34]. We calculated the adsorption energy (E_{ads}) of different species on the surface as follow,

$$E_{ads} = E_{OH/surf} - E_{surf} - E_{OH(g)} \tag{3}$$

where $E_{OH/surf}$ and E_{surf} are the energies of substrate with and without OH adsorption, and $E_{OH(g)}$ is the energy for isolated OH.

3 Results and discussion

The typical synthesis procedure of Ni_3S_2-MoS_2/NC is illustrated in Scheme 1. Na_2MoO_4, CS, and CH_4N_2S serve as the molybdenum source, carbon/nitrogen source, and sulfur source, respectively. Initially, polymeric chains of CS were immersed in an acetic acid solution. This process activates the positively charged NH_3^+ groups, which have the capacity to adhere to the negatively charged MoO_4^{2-} species via a combination of electrostatic forces and hydrogen bonds. This interaction initiates the catalytic process for the polymerization of CS upon the addition of a molybdenum source [35]. Subsequently, the pre-cleaned Ni foam was transferred into the acidic gel with a cross-linked network structure, promoting the generation of Ni^{2+} ions. In the hydrothermal process, the MoO_4^{2-} was adsorbed on the CS molecular chains, while Ni^{2+} was interacted with H_2S released from thiourea, evoking the *in situ* nucleation and

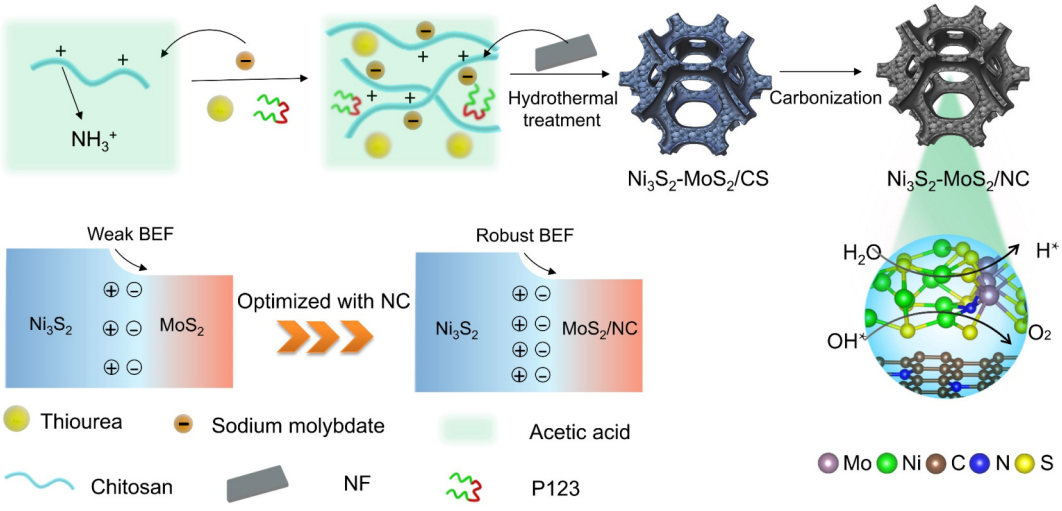

Scheme 1 Schematic illustration of the construction process of Ni_3S_2-MoS_2/NC.

growth of Ni_3S_2-MoS_2/CS. Finally, the CS component was transformed into a NC structure after carbonizing Ni_3S_2-MoS_2/CS under an inert atmosphere. Therefore, by adjusting the chitosan feeding, we effectively regulate the BEF intensity of Ni_3S_2-MoS_2 through controlled modulation of the Mo–N configuration between MoS_2 and NC. Meanwhile, the carbon skeleton effectively prevents MoS_2 from agglomerating and leaching under strong alkaline conditions, empowering the robust BEF for the electrocatalytic reaction.

The hierarchical structure and crystalline phase of the samples were characterized using XRD and transmission electron microscopy (TEM) techniques. The peaks at around 14.5°, 33.4°, 58.5°, and 60.4° are well indexed as (002), (101), (110), and (008) planes of MoS_2 (PDF No. 37-1492) [36], whereas the peaks located at 21.7°, 31.1°, 37.7°, 38.3°, 49.7°, 50.1°, and 55.1° are unambiguously corresponding to Ni_3S_2 (PDF No. 44-1418) [37] in Ni_3S_2-MoS_2 and Ni_3S_2-MoS_2/NC-0.45 (Fig. 1(a)). Notably, the peak located at 26° is identified as (100) plane of graphitic carbon in the Ni_3S_2-MoS_2/NC-0.45, verifying that NC is successfully coupled with Ni_3S_2-MoS_2 heterojunction. The fingerprint characteristics of carbon are further confirmed by Raman spectrum (Fig. S1 in the Electronic Supplementary Material (ESM)), where the D band (1350 cm^{-1}) and G band (1590 cm^{-1}) correspond to structural defects and disordered carbon, respectively. Additionally, the (002) peak of MoS_2 phase in Ni_3S_2-MoS_2/NC-0.45 is weaker than that of Ni_3S_2-MoS_2 moiety, indicating the less layer stacking of MoS_2 in Ni_3S_2-MoS_2/NC-0.45 [38]. The Ni_3S_2-MoS_2 particles are uniformly embedded on the amorphous NC framework to form a well-defined conductive network, which is beneficial for improving electrical contact and catalysts dispersion (Fig. 1(b)). The carbon layer, responsible for large surface areas and interconnected passages, is beneficial for ion diffusion/transport and electrolyte penetration, which could facilitate the ion accessibility in the entire electrode. Further high-resolution TEM (HRTEM) image (Fig. 1(c)) exhibits distinct lattice fringes and the interface between the Ni_3S_2 and MoS_2 phases. More detailed HRTEM image (Fig. S2 in the ESM) shows that the lamellar MoS_2 consisting of few layers is distributed on the carbon layer, which provides abundant active edge sites for electrochemical reactions. The *d*-spacing of 0.23 nm can be indexed to the (021) plane of Ni_3S_2, and the interplanar distance of 0.65 nm can be attributed to the (002) plane of hexagonal MoS_2, which confirms the successful construction of the Ni_3S_2-MoS_2 heterojunction. Such an intimate lattice boundary, marked with a red dashed line without any defects, induces strong electronic interaction at the interface and thus could enhance the electrocatalytic performance. The strong coupling at the interface also accelerates the electron movement and maximizes the utilization of charge carriers. According to the selected area electron diffraction (SAED) pattern (Fig. 1(d)), a polycrystalline structure is revealed by a series of diffraction rings, which can be attributed to the (104), (113), and (201) crystalline planes of Ni_3S_2 and (116), (114), (004), and (002) crystalline planes of MoS_2. The atomic distribution model clearly demonstrates the 2H MoS_2 phase (Fig. 1(e)), where the purple and yellow balls refer to Mo and S atoms, respectively. The corresponding fast Fourier transform (FFT, Fig. 1(f)) pattern showcases the rotational angle ca. 10° between individual nanodomains, representing a flawless crystal for fast electron transport [39]. Moreover, the TEM mapping of Ni_3S_2-MoS_2/NC-0.45 shows that the Ni, Mo, N, C, and S elements are evenly distributed among the whole regions (Fig. 1(g)), illustrating the N element is doped into the Ni_3S_2-MoS_2 heterojunction. The mass ratio of Mo, Ni, and S elements in Ni_3S_2-MoS_2/NC-0.45 sample is determined from ICP measurement, which is 1:17.6:4.8.

To investigate the interfacial interaction of Ni_3S_2-MoS_2/NC-0.45, XPS was applied to analyze the electronic structures. The full XPS spectrum (Fig. S3 in the ESM) reveals the appearance of Ni, Mo, C, S, and N elements in Ni_3S_2-MoS_2/NC-0.45, which is in agreement with the results of TEM mapping. The N 1s spectrum of Ni_3S_2-MoS_2/NC-0.45 reveals three distinct peaks at 395.4, 398.1, 399.3, and 401.1 eV (Fig. 2(a)), corresponding to Mo–N, pyridinic N, pyrrolic N, and graphitic N species, respectively [40, 41]. The formation of Mo–N bond is believed to stabilize MoS_2 [42], which relieves electron clouds localization and leads to charge redistribution. In high-resolution Ni 2p spectrum of Ni_3S_2-MoS_2/NC-0.45 (Fig. 2(b)), the fitted doublet peaks ca. 855.2/872.7, 856.4/874.1, and 861.5/879.8 eV are attributed to Ni^{2+}, Ni^{3+}, and satellite peaks, respectively [43]. In particular, the binding energy of the Ni^{3+} signal in Ni_3S_2-MoS_2/NC-0.45 shifts to a higher value compared to other references, indicating the strong electron transfers from Ni_3S_2 to MoS_2 after compositing NC into the Ni_3S_2-MoS_2 heterostructure. As a result, the Ni_3S_2-MoS_2/NC-0.45 catalyst exhibits the highest Ni^{3+}/Ni^{2+} ratio among all the investigated

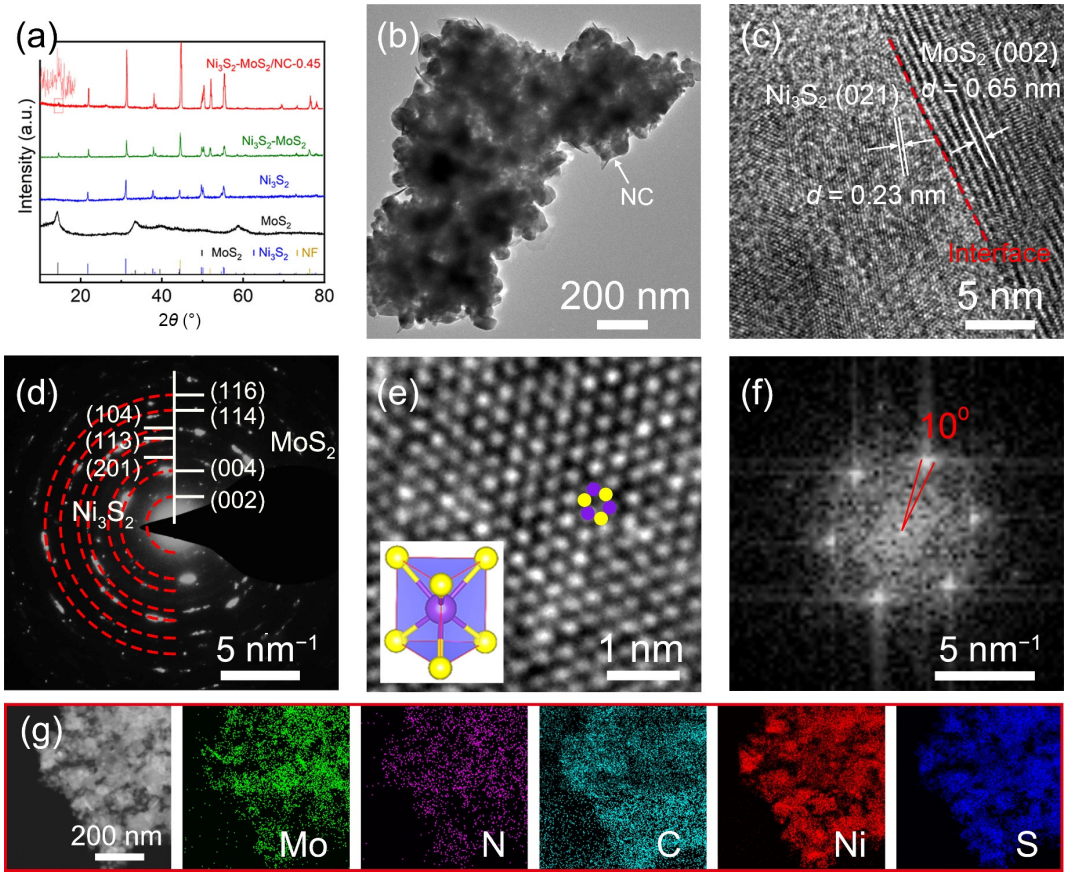

Figure 1 (a) XRD patterns of different samples. (b) TEM image, (c) HRTEM image, and (d) SAED pattern of Ni_3S_2-MoS_2/NC-0.45. (e) Enlarged HRTEM image of MoS_2 phase and (f) the corresponding FFT pattern in Ni_3S_2-MoS_2/NC-0.45. (g) TEM mapping of Ni_3S_2-MoS_2/NC-0.45.

catalysts (Fig. 2(c)), which would facilitate OH^- adsorption through the electrostatic effect. The deconvoluted Mo 3d profiles (Fig. 2(d)) clearly display the dominating Mo^{4+} signals of Mo $3d_{5/2}$ and Mo $3d_{3/2}$ at binding energy of 229.4 and 232.6 eV, respectively, indicating the electron-rich state of Mo with low valence state configuration [42]. The remaining two weak peaks belong to the S 2s (226.7 eV) and Mo^{6+} (235.4 eV), where the most negative shift of Mo^{6+} binding energy further verifies the strong interfacial electron migration in Ni_3S_2-MoS_2/NC-0.45, leading to strong polarization and BEF at the interface between Ni_3S_2 and MoS_2. This electron transfer behavior can be elucidated by the crystal-field theory [44]. The S atoms typically serve as a weak field ligand, which endow Ni and Mo elements with the high spin states of $t_{2g}^6e_g^2$ and $t_{2g}^3e_g^1$, respectively. The doping of N atoms with high electronegativity into MoS_2 in the heterojunction facilitates the transfer of electrons from the t_{2g} orbital of Ni to the vacant e_g orbital of Mo through the interface bond of the Mo–Ni–S bridge (Fig. 2(e)). Besides, the electronic configurations for the valence states of Ni are usually characterized as $3d^7$ ($t_{2g}^6e_g^1$) for Ni^{3+} and $3d^8$ ($t_{2g}^6e_g^2$) for Ni^{2+} [45]. The Ni^{3+} ions engage in a π-donation interaction with bridging O^{2-} ions, facilitated by the unpaired electrons present in the π-symmetry t_{2g} d-orbitals [46]. Alternatively, the interaction between Ni^{2+} and the O^{2-} ions is predominantly repulsive due to the complete occupancy of the π-symmetry t_{2g} d-orbitals. The bond order for each intermediate species bound to Ni^{2+} and Ni^{3+} has been evaluated (Fig. 2(f)). Influenced by spin-orbital coupling, the bond orders for the OH*, O*, and OOH* intermediates with Ni^{3+} are identified as 1, 1.5, and 1, respectively. Conversely, for Ni^{2+}, these bond orders are 0.5, 1.5, and 0.5, respectively. The elevated bond orders associated with Ni^{3+} imply a robust orbital interaction between the Ni^{3+} ions and the intermediates of OER. Consequently, the activity of the OER may be enhanced in Ni_3S_2-MoS_2/NC-0.45 due to its dominant Ni^{3+} content. Moreover, the strong BEF would induce Ni sites with electron delocalization for OH^- adsorption, promoting the dissociation of H–OH [17, 47, 48].

The chemical composition and bonding characteristics of catalysts were further confirmed by Raman spectrum (Fig. 3(a)). The signals at 380.1, 405.4, and 450.3 cm^{-1} are attributed to the in-plane E_{2g}^1, out-of-plane A_{1g} and 2LA(K–M) phonon vibrational modes of 2H MoS_2 phase, respectively [49]. The Raman peaks at around 184.1, 197.6, 220.5, 240.5, 301.8, and 346.7 cm^{-1} are ascribed to Ni_3S_2 [50, 51]. Notably, the peak regarding A_{1g} vibration mode behaves a blue shift, and the intensity ratio of A_{1g}/E_{2g}^1 in Ni_3S_2-MoS_2/NC-0.45 is increased after introducing NC into the Ni_3S_2-MoS_2 heterojunction, which can be ascribed to the presence of a Mo–N bond [52, 53]. Notably, the absence of Ni–N signals around 500 cm^{-1} indicates negligible N dopants in Ni_3S_2 lattice [54]. This observation can be mainly attributed to the electrostatic repulsion between Ni cations and NH_3^+, which blocks Ni–N bond formation. Additionally, the large layer spacing with an adequate reaction space of S–Mo–S in MoS_2 favors the doping of N atoms over S–Ni–S in Ni_3S_2 counterpart. To gain a more comprehensive insight into the N-coordinated environment and electronic structure in Ni_3S_2-MoS_2/NC-0.45, the electron transfer phenomenon was analyzed based on XAFS spectra at the Mo K-edge. However, the Ni foam substrate exhibits a pronounced self-

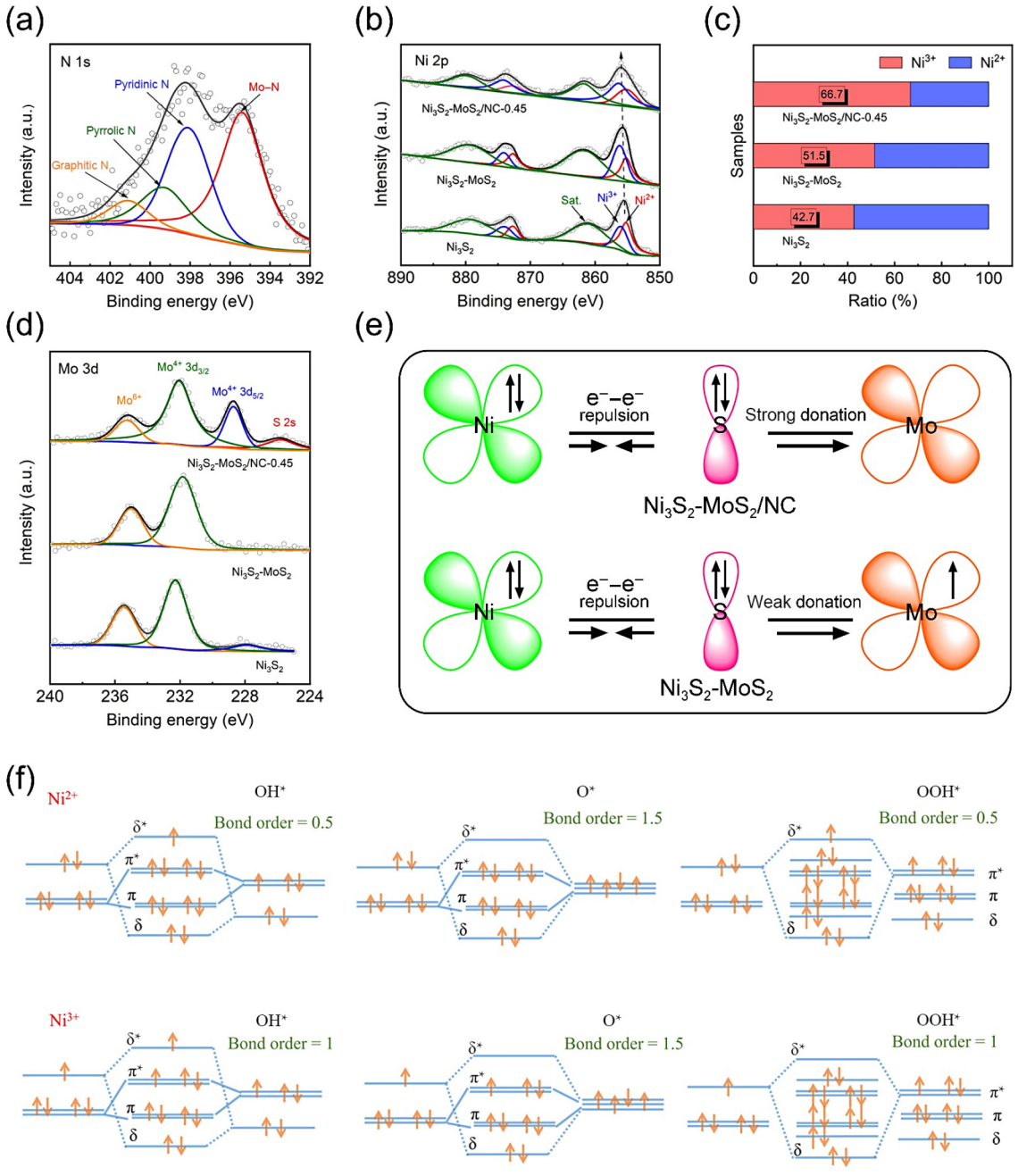

Figure 2 (a) High-resolution XPS spectrum of N 1s in Ni_3S_2-MoS_2/NC-0.45. (b) High-resolution XPS spectra of Ni 2p, (c) Ni cation ratios, and (d) high-resolution XPS spectra of Mo 3d of different catalysts. (e) The electronic coupling between Mo and Ni in Ni_3S_2-MoS_2/NC and Ni_3S_2-MoS_2. (f) The orbital interactions between Ni cations and the OER intermediates.

absorption effect, which tends to mask the Ni signals emanating from the catalyst layer. Therefore, the Ni K-edge of XANES curves are absent from the analysis. As demonstrated by the Mo K-edge of XANES curves (Fig. 3(b)), the Mo K-edge position of Ni_3S_2-MoS_2/NC-0.45 shifts to a lower energy compared to those of Ni_3S_2-MoS_2 and MoS_2, suggesting the strong electron transfer occurs from Ni_3S_2 to MoS_2 after introducing NC, which is well consistent with the XPS results. As observed from the Fourier transform k^2 weighted Mo K-edge XAFS of Ni_3S_2-MoS_2/NC-0.45, the main peaks located at about 1.5, 2.0, and 2.7 Å correspond to the Mo–N, Mo–S, and Mo–Mo paths, respectively (Fig. 3(c)), which further confirms the Mo–N bond formation. Compared with the Mo–S peak of MoS_2 and Ni_3S_2-MoS_2, the characteristic Mo–S peak of Ni_3S_2-MoS_2/NC-0.45 shifts to a longer radial distance, suggesting the more electron transfers to Mo [55–58], consistent with XPS and Raman results. The weaker amplitude of the Mo–S peak in Ni_3S_2-MoS_2/NC-0.45 than that of Ni_3S_2-MoS_2 further verifies the N element is doped in Ni_3S_2-MoS_2 heterojunction after coupling with NC. To discern the structure information at the Mo K-edge among various samples, the wavelet transform (WT) analysis on the extended X-ray absorption fine structure (EXAFS) oscillations is adopted due to its high resolution in both k and R spaces [59]. Notably, the WT contour plot for the Ni_3S_2-MoS_2/NC-0.45 sample exhibits significant intensity peaks at R = 1.5 Å, which substantiates

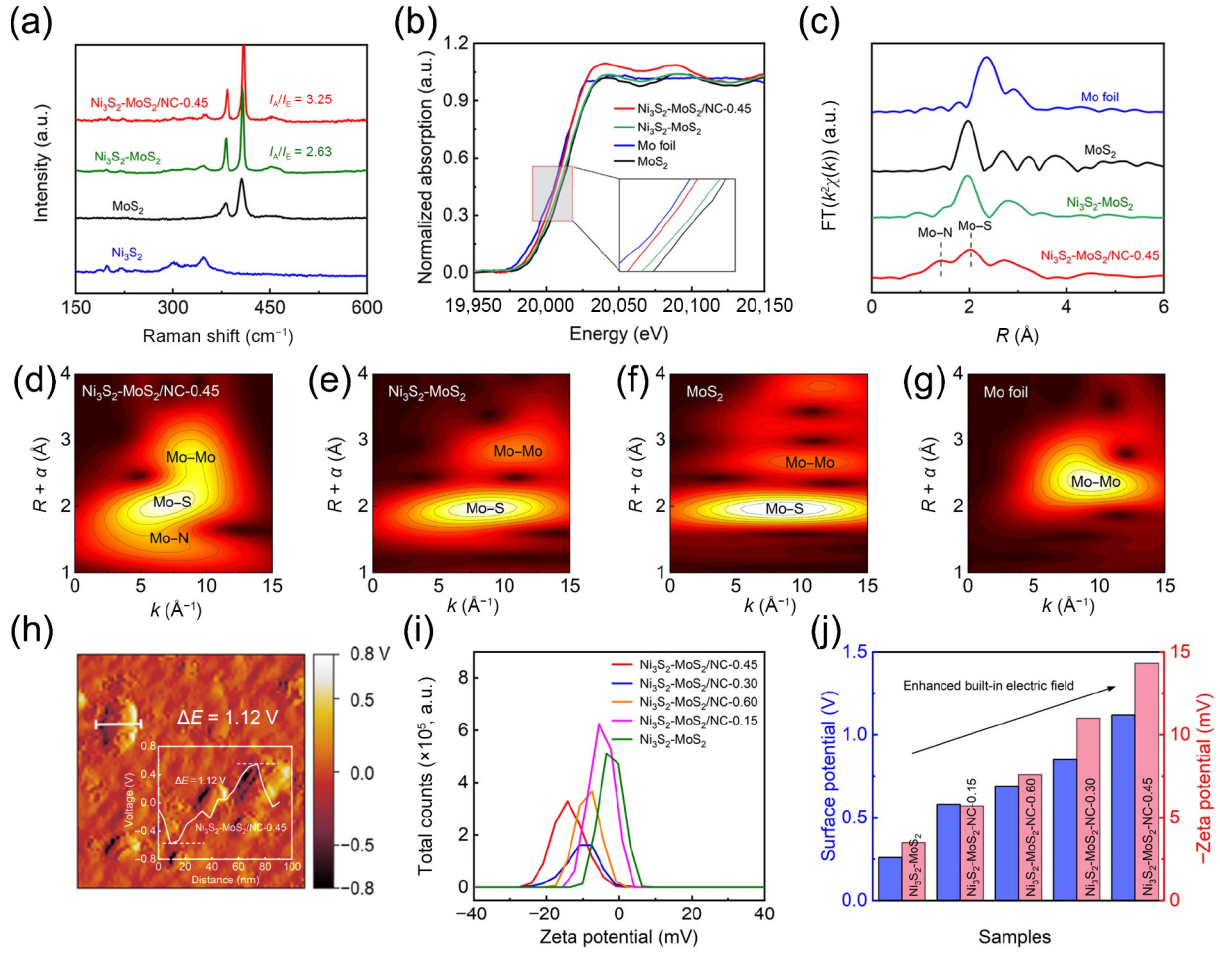

Figure 3 (a) Raman spectra of different samples. (b) XANES, (c) FT-EXAFS, and (d)–(g) k^2-weighted WT-EXAFS contour plots of different samples at Mo K-edge. (h) KPFM potential image of Ni_3S_2-MoS_2/NC-0.45. (i) Zeta potential and (j) comparison of BEF intensity of different samples.

the presence of Mo–N contribution (Fig. 3(d)). Comparatively, the Mo–S bond peak in Ni_3S_2-MoS_2/NC-0.45 shifts to the lower k value than those of references (Figs. 3(e)–3(g)), indicating the structural evolution after coupling NC. The significant changes in the Mo oscillation can be also observed in Fig. S4 in the ESM, signifying a different local atomic environment for the N atoms in Ni_3S_2-MoS_2/NC-0.45 and thus promoting the redistribution of interface electrons. This observed strong interfacial electron interaction can be induced by the robust BEF. To prove this conclusion, the BEF of the as-prepared catalysts was measured according to the following equation [60]

$$F_s = (-2V_s\rho/\varepsilon\varepsilon_0)^{1/2} \quad (4)$$

where F_s, V_s, and ρ represent the magnitude of the BEF, surface voltage, and surface charge density, respectively. The values of ε and ε_0 denote the low-frequency dielectric constant and vacuum permittivity, respectively. Therefore, the BEF is primarily influenced by V_s and ρ. Consequently, a quantitative assessment of the BEF intensity can be made by comparing the values of $(V_s\rho)^{1/2}$, where the parameters of V_s and ρ can be determined using KPFM and zeta potential measurements, respectively. The corresponding line-scanning surface potential profiles indicate that the contact potential difference (Fig. 3(h)) of Ni_3S_2-MoS_2/NC-0.45 (1.12 V) was much higher than those of other heterojunctions (Fig. S5 in the ESM), demonstrating an intensified surface potential for Ni_3S_2-MoS_2/NC-0.45. Additionally, the zeta potential of Ni_3S_2-MoS_2/NC-0.45 was also higher than those of other counterparts (Fig. 3(i)), delivering the largest surface potential and stability in an aqueous solution [61]. The quantitative results provided in Fig. 3(j) verify the intensified BEF of the Ni_3S_2-MoS_2/NC-0.45 heterostructure. Such a BEF is anticipated to contribute to stabilizing catalysts and simultaneously augmenting the electrocatalytic activity at the interfacial active sites [62], which could effectively avoid the dissolution of active species in harsh solutions. Therefore, the high-electronegativity N doping in MoS_2 can intensely capture electrons from Ni_3S_2, and the target heterostructure presents lower charge migration resistance and forms the well-defined nucleophilic and electrophilic sites, corroborating that the improvement mechanism of N doping is largely attributed to the enhanced strength of BEF at the interface between MoS_2 and Ni_3S_2. It is noteworthy that the BEF of the Ni_3S_2-MoS_2/NC-0.60 sample exhibits a decreasing trend, which may be attributed to excessive N doping that induces ample lattice defects in MoS_2, resulting in adverse effects at the interface.

The LSV technique was employed to evaluate the alkaline HER activity of the synthesized catalysts. The polarization curve of the Ni_3S_2-MoS_2/NC-0.45 sample (Fig. 4(a)) proceeds rapidly to achieve a current density of −10 mA·cm^{-2} with a relatively low overpotential of 75 mV. In contrast, the other samples, including Ni_3S_2-MoS_2/NC-0.30, Ni_3S_2-MoS_2/NC-0.60, Ni_3S_2-MoS_2/NC-0.15, Ni_3S_2-MoS_2, Ni_3S_2, and MoS_2 exhibit higher overpotentials of 98, 109, 138, 154, 171,

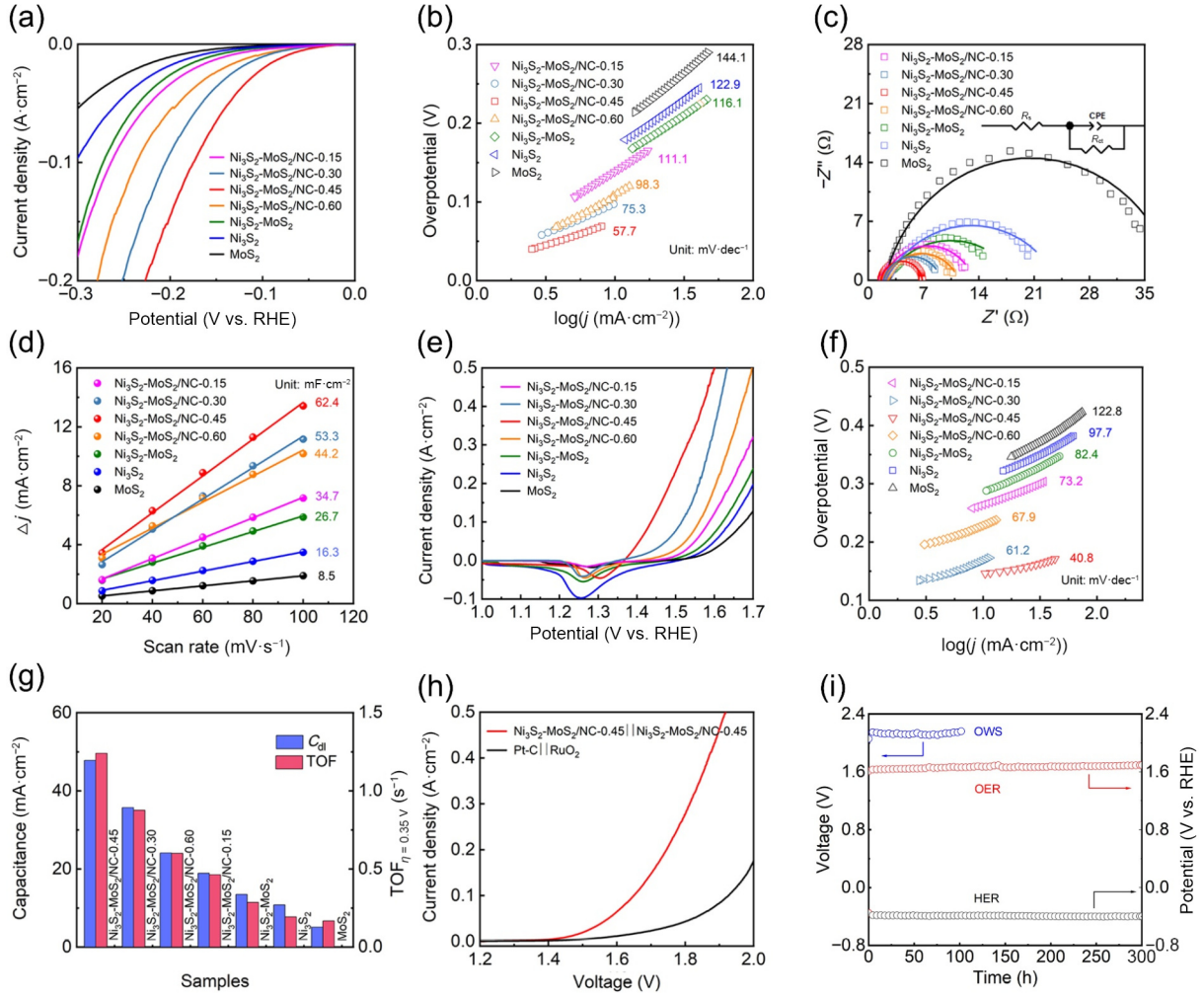

Figure 4 (a) LSV curves, (b) Tafel plots, (c) EIS plots, and (d) C_{dl} values of different electrodes for HER. (e) LSV curves, (f) Tafel plots, and (g) C_{dl} and TOF values of different electrodes for OER. (h) LSV curves of different electrodes for OWS. (i) CP curves of Ni_3S_2-MoS_2/NC-0.45 electrode at 0.2 A·cm^{-2}.

196 mV, respectively. These findings underscore the positive impact of heterojunction integration on HER performance, which correlates well with the strength of BEF. The dynamics and underlying mechanisms of the HER were further elucidated through Tafel plot analysis (Fig. 4(b)). Under alkaline conditions, the HER typically involves a two-step process, which can follow either the Volmer–Tafel or the Volmer–Heyrovsky pathway. The Ni_3S_2-MoS_2/NC-0.45 sample views a Tafel slope of 57.7 mV·dec^{-1}, indicating a more rapid HER rate governed by the Volmer–Heyrovsky mechanism. To further analyze the intrinsic charge transport properties of these samples, the EIS spectra of all samples were fitted using the equivalent circuit (Fig. 4(c) and Table S1 in the ESM). The Nyquist plot of the Ni_3S_2-MoS_2/NC electrode shows a well-defined semicircle with the smallest charge transfer resistance (R_{ct}) of 5.2 Ω, enabling faster electron transport kinetics caused by the enhanced BEF in the heterojunction. The ECSA was estimated from the double-layer capacitance (C_{dl}), based on its linear relation. Therefore, the C_{dl} value was evaluated through CV measurements at different scan rates (Fig. 4(d) and Fig. S6 in the ESM). The C_{dl} of 62.4 mF·cm^{-2} for Ni_3S_2-MoS_2/NC-0.45 is 1.2–7.3 times larger than that of other investigated catalysts, implying that the robust BEF can effectively expose electroactive sites for the Ni_3S_2-MoS_2/NC-0.45 moiety. To eliminate the contribution of ECSA, normalizing current density by ECSA provides a more accurate method for assessing intrinsic catalytic activity. As expected, the Ni_3S_2-MoS_2/NC-0.45 electrode demonstrates the highest current density after ECSA normalization (Fig. S7 in the ESM), which possesses superior intrinsic catalytic activity compared to other catalysts for HER. The TOF value for HER, representing the number of reactions per active site per second, was calculated through the estimated number of the active sites to assess the intrinsic activity of their active sites in PBS solution (Fig. S8 in the ESM). The Ni_3S_2-MoS_2/NC-0.45 electrode achieves an exceptional TOF value of 0.83 s^{-1} at an overpotential of 200 mV (Fig. S9 in the ESM), significantly surpassing other catalysts and thus demonstrating its superior intrinsic activity. The complementary half-reaction of OER in water splitting also acts as another major bottleneck, which was further analyzed in 1 M KOH. Note that the reverse scan mode for OER polarization curves was conducted to avoid oxidative peak interferences. From the OER polarization curves of Ni_3S_2-MoS_2/NC-0.45 electrode (Fig. 4(e)), current densities at 10 and 200 mA·cm^{-2} were achieved at low overpotentials of 146 and 255 mV, respectively. The ranking of OER activities among all the catalysts follows the order of Ni_3S_2-MoS_2/NC-0.45 > Ni_3S_2-MoS_2/NC-0.30 > Ni_3S_2-MoS_2/NC-0.60 > Ni_3S_2-MoS_2/NC-0.15 > Ni_3S_2-MoS_2 > Ni_3S_2 > MoS_2. The obvious OER activity gap in different heterojunctions strongly confirms that the excellent performance is derived from BEF differences. For a

deeper understanding of the OER performance, the Ni_3S_2-MoS_2/NC-0.45 electrode witnesses the smallest Tafel slope (40.8 mV·dec^{-1}) among the anodes (Fig. 4(f)), validating its fast catalytic kinetics. Additionally, EIS results (Fig. S10 and Table S2 in the ESM) demonstrate the favorable charge transfer mobility of the Ni_3S_2-MoS_2/NC-0.45 electrode during the OER. Such a strong BEF provides a highway for continuous electron flow and enhances the utilization of active sites. Similarly, the Ni_3S_2-MoS_2/NC-0.45 electrode also exhibits the highest C_{dl} value up to 47.8 mF·cm^{-2} (Fig. 4(g) and Fig. S11 in the ESM), exposing the more active sites under strong BEF. The TOF values of various electrodes at 1.58 V clearly indicate that Ni_3S_2-MoS_2/NC-0.45 is the most efficient OER catalyst with the highest atomic utilization efficiency (Fig. 4(g)). Moreover, the Ni_3S_2-MoS_2/NC-0.45 electrode possesses the largest current density after being normalized by ECSA for OER, exhibiting the highest specific activity among all samples (Fig. S12 in the ESM). The Ni_3S_2-MoS_2/NC-0.45 electrode exhibits the best catalytic activity in various indicators, which is well matched with the BEF intensity.

Motivated by the exceptional performance of the Ni_3S_2-MoS_2/NC-0.45 electrode in both HER and OER when tested in a 1.0 M KOH solution, this electrode material was subsequently utilized to construct a two-electrode system for OWS. This cell system achieves current densities of 10 and 200 mA·cm^{-2} at the respective potentials of 1.45 and 1.75 V for the Ni_3S_2-MoS_2/NC-0.45 electrode (Fig. 4(h)). To estimate the electron utilization efficiency during water splitting, the Faradaic efficiency of the Ni_3S_2-MoS_2/NC-0.45 electrode was calculated by collecting the gases escaping from the anode and cathode using a gas-tight H-type electrolyzer device with a drainage system. The collected volume ratio of H_2 to O_2 is close to 2, which aligns with the theoretical result (Fig. S13(a) in the ESM). The average Faradaic efficiency of Ni_3S_2-MoS_2/NC-0.45 electrode was measured to be over 95% (Fig. S13(b) in the ESM), indicating highly efficient conversion on this electrode. The Ni_3S_2-MoS_2/NC-0.45 electrode demonstrates remarkable stability at −0.2 A·cm^{-2} as evaluated by CP tests, which maintains 97.2% of the initial current with only a minor decrease in activity after 300 h operation. The crystal structure and morphology of the Ni_3S_2-MoS_2/NC-0.45 electrode were investigated by TEM after the HER stability test. The Ni_3S_2-MoS_2 nanoparticles remain firmly anchored on the NC (Fig. S14(a) in the ESM), indicating good structural stability. The HRTEM image further reveals that the heterojunction interface remains intact (Fig. S14(b) in the ESM), while the SAED pattern exhibits distinct diffraction rings (Fig. S14(c) in the ESM), confirming the well-defined crystallinity with the NC protection. Compared with fresh electrodes, no significant component change is observed after HER durability (Fig. S15(a) in the ESM). For the N 1s region, the Mo–N bond is preserved (Fig. S15(b) in the ESM), and the oxidation states of Ni (Fig. S15(c) in the ESM) and Mo (Fig. S15(d) in the ESM) also exhibit minimal changes. All these observations confirm the robust stability of the Ni_3S_2-MoS_2/NC-0.45 catalyst. Similarly, the Ni_3S_2-MoS_2/NC-0.45 electrode also delivers an enduring stability at 0.2 A·cm^{-2}, where it retains its initial activity with a minimal potential increase over a 300 h OER operation. As a result, it sustains stable water splitting for 100 h at a substantial current density of 200 mA·cm^{-2} (Fig. 4(i)). The water splitting performance of the Ni_3S_2-MoS_2/NC-0.45 catalyst was compared with various other homogeneous heterojunctions, which is more competitive than most recently reported dual-functional electrocatalysts (Table S3 in the ESM) [63–72]. The remarkable catalytic performance, coupled with its high electrochemical stability, positions the Ni_3S_2-MoS_2/NC-0.45 electrode as a promising candidate for cost-effective and efficient water splitting, suitable for industrial-scale applications.

Experimentally, the vibration behavior of the O–H bonds in the H_2O molecules on the different samples was analyzed by Fourier transform infrared spectroscopy (FT-IR) (Fig. 5(a)). The intramolecular bending vibrations of the O–H bonds (ca. 1640 cm^{-1}) in the adsorbed water are visible in all samples. Notably, the Ni_3S_2-MoS_2/NC-0.45 demonstrates the most significant red-shift in its peak, which is indicative of the enlarged O–H bond lengths. This elongation implies that the O–H bonds in the H_2O molecules on Ni_3S_2-MoS_2/NC-0.45 are more susceptible to disruption, compared to those in other scenarios, thereby facilitating the dissociation of water molecules. Interestingly, the water dissociation ability of above materials is closely aligned with their BEF strength. This correlation is mainly attributed to the robust BEF in Ni_3S_2-MoS_2/NC-0.45, which induces Ni sites to lose more electrons, as evidenced by XPS and X-ray absorption spectroscopy (XAS) results. Consequently, the electron-deficient Ni sites broaden the d-band and elevate the Fermi level, leading to a lower energy level of the unoccupied states. As a result, the enhanced electronic coupling effect between the lowest unoccupied d orbitals of Ni_3S_2 and the highest occupied p orbitals of H_2O molecule is desirably to accelerate water dissociation kinetics [73]. Moreover, the water dissociation process is accompanied by continuous electron consumption, so the robust BEF promotes electron transfer at electroactive sites. Further insight into the structural integrity of the Ni_3S_2-MoS_2/NC-0.45 catalyst was obtained through Raman spectroscopy after durability test, which displays that the peaks associated with the Ni–S and Mo–S bonds remain unchanged even after an extended period of HER (Fig. 5(b)). Besides, the characteristic peak of carbon shows minimal change after the stability test, indicating its excellent resistance to alkaline corrosion and effectively preserving the original heterostructure. Based on the above results, it should be concluded that the Ni_3S_2-MoS_2/NC-0.45 catalyst effectively enhances water dissociation due to the easy polarization of the polar H_2O molecule under the strong BEF, while the carbon layer is hypothesized to prevent the loss of active components during the HER process.

To uncover the essential active species and discern the link between structure and activity during OER, Raman spectroscopy, XAS, and TEM tests were performed on the Ni_3S_2-MoS_2/NC-0.45 sample. The Raman signals (Fig. 5(b)) attributed to Ni–S and Mo–S vibrations are still visible after the durability test, and peaks corresponding to the Ni–O bond (560 cm^{-1}) in NiOOH and the Mo–O bond (740/820 cm^{-1}) in MoO_x have been detected [74–76]. The *ex situ* Raman test was adopted to track the dynamic evolution of active species and assess the impact of the BEF during OER. The potential-dependent Raman signal of Ni_3S_2-MoS_2/NC-0.45 (Fig. 5(c)) at approximately 520 cm^{-1} corresponds to the Ni–O stretching vibrations in $Ni(OH)_2$, whereas the Mo–O bonds in MoO_x become evident at the potential of 1.35 V. As the applied potential increases, the intensity of the Mo–O signals is gradually increasing, and the $Ni(OH)_2$ phase transitions to the active NiOOH phase. In contrast, the Raman signal from Ni_3S_2-MoS_2 exhibits a low activity of the $Ni(OH)_2$ phase until the potential reaches 1.65 V, whilst the Ni_3S_2 and MoS_2 phases are completely absent under strong alkaline solution. This indicates that an unstable

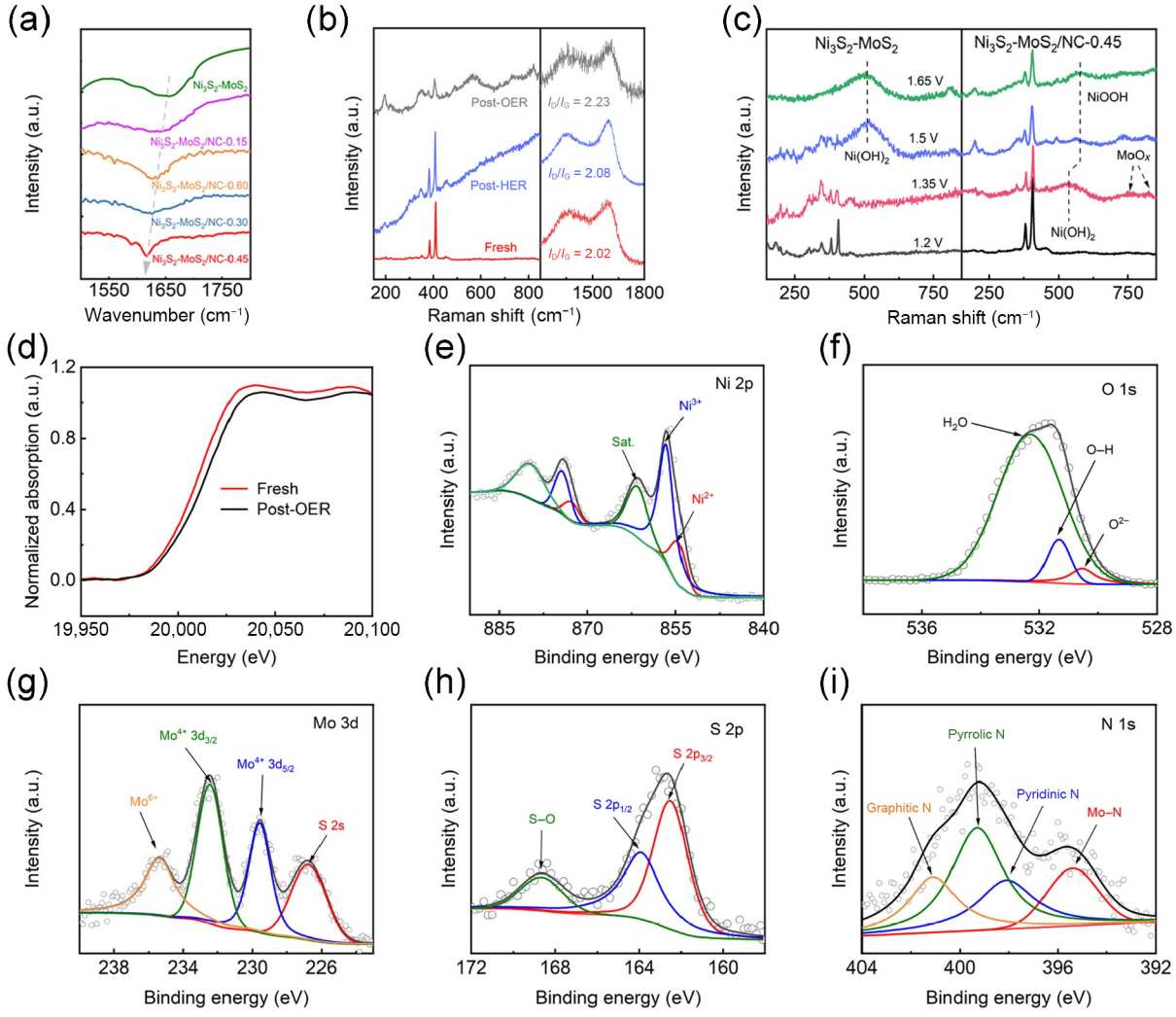

Figure 5 (a) FT-IR spectra of different electrodes. (b) Raman spectra of Ni_3S_2-MoS_2/NC-0.45 electrode before and after HER/OER. (c) Potential-dependent Raman spectra of Ni_3S_2-MoS_2/NC-0.45 and Ni_3S_2-MoS_2 electrodes. (d) XANES spectra of Ni_3S_2-MoS_2/NC-0.45 electrode before and after OER at Mo K-edge. XPS spectra of (e) Ni 2p, (f) O 1s, (g) Mo 3d, (h) S 2p, and (i) N 1s for the Ni_3S_2-MoS_2/NC-0.45 electrode after OER.

heterostructure in Ni_3S_2-MoS_2 significantly hampers OER activity. Note that the impetus for surface reconstruction stems from anisotropy of the surface free energy. Crafting heterojunctions with a robust BEF serves as an effective strategy for adjusting the surface energy at the surface, hinting at its prospective use in hastening the reformation process [77].

Concurrently, the XAFS spectrum at the Mo-edge shows a positive shift in the edge position, further validating that the Mo atom experiences an oxidation process (Fig. 5(d)) during OER. The corresponding FT-EXAFS plot of Ni_3S_2-MoS_2/NC-0.45 exhibits a slightly negative shift in the Mo–N shell (Fig. S16 in the ESM), which could be ascribed to the slight oxidation behavior of Mo, as reflected by the Raman spectra. The corresponding post-OER electrode exhibits a robust structure, where the Ni_3S_2-MoS_2 nanoparticles are well dispersed on the NC (Fig. S17(a) in the ESM). The HRTEM image still witnesses a clear heterointerface (Fig. S17(b) in the ESM) even after the Ni_3S_2-MoS_2/NC-0.45 electrode underwent the strong oxidation reaction, indicating that the robust BEF is preserved. Additionally, the oxidation layer (ca. 2 nm) composed of MoO_3 and NiOOH at the Ni_3S_2-MoS_2 surface can be detected in Fig. S17(c) in the ESM, suggesting that the surface reconstruction occurs during OER operation. The SAED pattern primarily shows the polycrystalline phases of Ni_3S_2 and MoS_2 (Fig. S17(d) in the ESM), implying a low surface reconstruction degree or that the surface mainly exists in an amorphous phase. The alterations in the chemical and electronic configurations of the Ni_3S_2-MoS_2/NC-0.45 electrode were evaluated using XPS after OER durability test. The detection of all elemental signals indicates that this catalyst possesses excellent stability (Fig. S18 in the ESM). The binding energy of Ni 2p spectrum in post-OER sample (Fig. 5(e)) shifts to a positive value, while the Ni^{3+} in NiOOH signal become more dominant (77.9%) due to surface oxidation. The newly formed NiOOH species exhibit excellent OER performance because their higher valence state enhances OH* affinity [78]. Further evidence for this phase transitions is revealed by the post-OER O 1s spectrum (Fig. 5(f)), which categorizes the oxygen species into three groups: O^{2-}, hydroxyl groups, and adsorbed H_2O [79]. The presence of O^{2-} peak suggests partial oxidation of the metal at the surface. Similarly, the enhancement of the Mo^{6+} signal from 15.6% to 21.4% in the Mo 3d spectrum (Fig. 5(g)) points to the conversion of Mo to its oxide state upon OER operation. In contrast, the S 2p signal witnesses almost no

change, possibly because NC suppressed the leaching of S element to a certain extent (Fig. 5(h)). As for the N 1s spectrum (Fig. 5(i)), the Mo–N signal persists after prolonged operation, indicating the stable crystal structure to keep the robust BEF. The findings collectively suggest that the Ni_3S_2-MoS_2/NC surface has been transformed into NiMo (oxy)hydroxide species during the OER process. This newly formed hybrid structure facilitates electron transfer from the internal Ni_3S_2-MoS_2 to the outer NiOOH/MoO_x catalytic layer, and the robust heterojunction shielded by a carbon layer is responsible for the enhanced OER activity. Based on the comprehensive analysis, we infer that the robust BEF in Ni_3S_2-MoS_2/NC-0.45 contributes to OH^- adsorption and thus facilitates surface reconstruction during OER.

To further elucidate the mechanisms behind the exceptional water splitting capabilities of the Ni_3S_2-MoS_2/NC-0.45 electrode, a suite of DFT calculations were conducted to investigate the intrinsic catalytic activity enhancements. The optimized Ni_3S_2-MoS_2/NC model witnesses 2.49 Å in Mo–S bond length (Fig. 6(a)), which is much larger than the Ni_3S_2-MoS_2 counterpart (Fig. S19 in the ESM), reflecting the strong electron-capturing capability of the Mo atom after being coordinated with N at the interface. The quantitative Bader charge analysis determines that the electron transfer numbers from Ni_3S_2 to MoS_2 are 0.32 and 0.70 eV for the Ni_3S_2-MoS_2 and Ni_3S_2-MoS_2/NC compositions, respectively (Tables S4 and S5 in the ESM). According to band theory, the electron transfer dynamics at the heterointerface are governed by the BEF potential, which is derived from the difference in work functions ($\Delta\Phi$) between different components across the interfaces [80, 81]. An intensified BEF potential facilitates rapid electron transfer, as indicated by a significant $\Delta\Phi$. As expected, the $\Delta\Phi$ between Ni_3S_2 and MoS_2 is increased from 0.69 to 0.93 eV after N atoms doping into MoS_2 lattice (Fig. S20 in the ESM). These results further validate that the nitrogen-doped MoS_2 lattice can significantly augment the BEF in the Ni_3S_2-MoS_2 composite by integrating with NC. The enhanced electron transfer number is known to create by the BEF, which serves as a highway for uninterrupted electron transfer, thereby boosting the efficiency of active site utilization. Furthermore, this redistribution of electron density is believed to lower the energy barriers for the adsorption and desorption of reaction intermediates, thus improving the electrocatalysis kinetics. It is conceivable that the electron-lacking Ni site can stabilize the adsorbed hydroxide species for facilitating the performance in both the HER and OER. As illustrated by the free energy profile of water dissociation (Fig. 6(b)), the Ni_3S_2-MoS_2 model exhibits the highest energy barrier for water dissociation (ΔG_w) of 2.27 eV, which corresponds to a significant kinetic impediment in the water splitting process, particularly affecting the rate of the initial electron transfer step in the HER. In contrast, the Ni_3S_2-MoS_2/NC model shows a substantially reduced ΔG_w to 1.65 eV, indicating a marked enhancement in the kinetics of water dissociation, which is essential for proton supply during the HER. Alternatively, the hydroxyl adsorption energy (E_{OH^*}) on the Ni sites for the Ni_3S_2-MoS_2/NC (Fig. 6(c)) and Ni_3S_2-MoS_2 (Fig. S21 in the ESM) models is determined to be −2.12 and −1.99 eV, respectively. This suggests that the Ni sites are more favorable for hydroxyl groups adsorption, ensuring a rapid kinetic rate for both the HER and OER processes.

To discern the challenges of surface reconstruction during OER, the ease of Ni binding to oxygen was evaluated by examining the Ni–O bond length. In the simulation of the oxidation process of Ni during OER, oxygen atom is attached to the Ni site on the

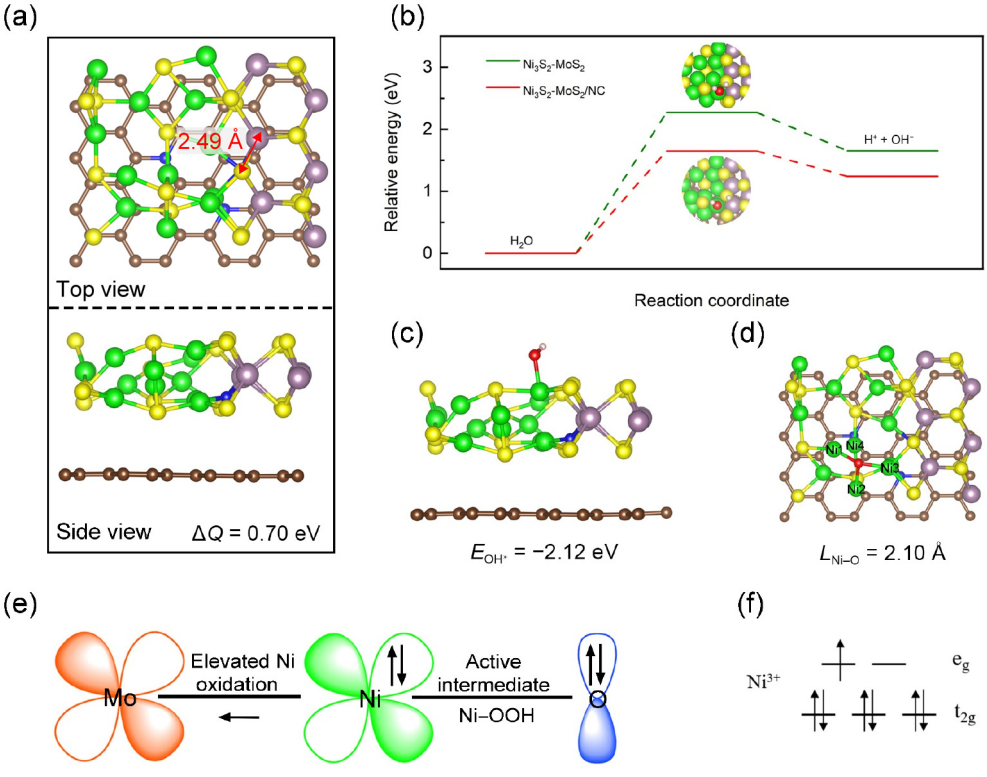

Figure 6 (a) The geometry optimization model and Bader charge analysis of Ni_3S_2-MoS_2/NC. (b) Free energy differences of Ni_3S_2-MoS_2 and Ni_3S_2-MoS_2/NC models for water dissociation. (c) The adsorption energies of OH^- on the Ni_3S_2-MoS_2/NC. (d) Ni_3S_2-MoS_2/NC pre-catalyst surface oxidation model. (e) The electron interaction between Mo and NiOOH. (f) The electron configuration of Ni^{3+}. The Ni, Mo, N, S, C, O, and H atoms are represented by green, purple, blue, yellow, brown, red, and pink spheres, respectively.

pre-catalyst surface [82]. As expected, the Ni–O bond length in the Ni_3S_2-MoS_2/NC model (Fig. 6(d)) is found to be 2.10 Å, which is shorter than that in the Ni_3S_2-MoS_2 model (Fig. S22 and Table S6 in the ESM). This indicates that the less stable Ni atoms influenced by a strong BEF are more inclined to form bonds with oxygen during the oxidation process, thus facilitating surface reconstruction. In the Ni–O–Mo unit, the electronic structure of Mo^{6+} possesses an unoccupied 4d orbital (Fig. 6(e)), which engages in π-donation with the O^{2-}. Therefore, a partial electron transfers from the Ni^{2+} to Mo^{6+} ion. This transfer transforms the electronic configuration of Ni^{2+} to that of Ni^{3+}. Commonly, a Jahn–Teller (JT) distortion is associated with Ni^{3+} due to the asymmetrical population of its electronically degenerate orbitals. As a result, the repulsion between the electrons in Ni^{3+} and O^{2-} is reduced, leading to a contraction of the Ni–O bond length. Furthermore, the e_g orbital of the Ni^{3+} is vacant due to the JT distortion (Fig. 6(f)), which renders OER more feasible at lower energy inputs.

The mechanism of water splitting on the Ni_3S_2-MoS_2/NC electrode, as deduced from experimental outcomes and DFT calculations, can be described as follows. The integration of NC within the Ni_3S_2-MoS_2 heterojunction results in N atoms being incorporated into MoS_2, which in turn enlarges the work function discrepancy between Ni_3S_2 and MoS_2, and thus intensifies its BEF. This strong BEF contributes to the electron-deficient Ni sites, facilitating the adsorption of hydroxyl groups during the HER/OER processes. In the case of HER, water molecules are first adsorbed onto the Ni sites at heterointerface. Subsequently, the HO–H bond is broken, allowing the hydrogen intermediates transfer to the S atoms in MoS_2, and thus H_2 is released. The strong BEF would induce the delocalization of the antibonding unoccupied orbitals of H_2O adsorbed on Ni sites, which results in an elevation of the O 2p orbital. This delocalization of the antibonding orbital of the O–H bonds in water facilitates the activation and cleavage of the O–H bond, thereby enhancing water dissociation. As for the OER process, the Ni sites in Ni_3S_2-MoS_2/NC feature the more positively charged centers by the BEF, which enhance the OH^- adsorption and facilitate the formation of NiOOH through a nucleophilic attack [83]. More specifically, the Ni_3S_2 progressively oxidizes to $Ni(OH)_2$ and NiOOH, while the MoS_2 undergoes oxidation to form MoO_x, accompanied by the leaching of S atoms. Consequently, the *in situ* formation of high-valence oxy/hydroxides on the surface of the pre-catalysts, combined with the high conductivity of the internal sulfides, significantly contributes to the outstanding performance of the OER.

4 Conclusions

In summary, our study presents the successful construction of a novel Ni_3S_2-MoS_2 heterojunction catalyst with an effectively modulated BEF through the introduction of NC. The robust BEF is imparted by coordinating the highly electronegative N element into the homologous heterojunction. The optimized heterojunction featured with a robust BEF delivers excellent HER and OER activity at 10 mA·cm^{-2}, with remarkably low overpotentials of 75 and 146 mV, respectively. This robust BEF persists even after 300 h operation under OER conditions in a strong alkaline solution. Experimental results and DFT calculations further confirm the robust BEF induces the high-valent Ni^{3+}, which accelerates water dissociation during HER and strengthens OH^- and surface reconstruction processes during OER. This strategy for optimizing homologous heterojunctions would provide a new platform for the qualitative regulation of active sites and new insights into the application of energy material for other homologous heterojunctions.

Electronic Supplementary Material: Supplementary material (including electrochemical measurements, XPS spectra, Raman spectra, KPFM images, DFT calculations, and TEM images) is available in the online version of this article at https://doi.org/10.26599/NR.2025.94907381 .

Data availability

All data needed to support the conclusions in the paper are presented in the manuscript and the ESM. Additional data related to this paper may be requested from the corresponding author upon request.

Acknowledgements

The authors gratefully acknowledge financial support from the National Key Research and Development Program of China (No. 2022YFB1105100), the National Natural Science Foundation of China (No. U2330105), and the funding from Science Foundation of China University of Petroleum, Beijing (No. 24620188JC005). We thank the 1W1B-XAFS Beamline of Beijing Synchrotron Radiation Facility (https://cstr.cn/31109.02.BSRF.1W1B) for providing technical support and assistance in XAFS data collection.

Declaration of competing interest

All the contributing authors report no conflict of interests in this work.

Author contribution statement

D. R. W.: Conceptualization, investigation, data curation, writing – original draft. S. W.: Conceptualization, software, methodology. H. N. Z.: Formal analysis, conceptualization. C. M. C.: Formal analysis, conceptualization. S. J. H.: Resources, conceptualization, supervision, project administration. P. Q.: Resources, conceptualization, software. L. R. Z.: Resources, conceptualization, software. Y. Y.: Resources, conceptualization, supervision, writing – review & editing, project administration, funding acquisition.

Use of AI statement

None.

References

[1] Wang, H.; Jiang, H. M.; Niu, Y. Q.; Siddiqui, N. A.; Khan, A.; Pan, L.; Lin, J. J. Three-dimensional structured of V-doped CoP *in situ* grown on MXene as highly efficient bifunctional electrocatalyst for water splitting. *Nano Res.* **2025**, *18*, 94907238.

[2] Shah, A. H.; Zhang, Z. S.; Huang, Z. H.; Wang, S. B.; Zhong, G. Y.; Wan, C. Z.; Alexandrova, A. N.; Huang, Y.; Duan, X. F. The role of alkali metal cations and platinum-surface hydroxyl in the alkaline hydrogen evolution reaction. *Nat. Catal.* **2022**, *5*, 923–933.

[3] Quan, L.; Jiang, H.; Mei, G. L.; Sun, Y. J.; You, B. Bifunctional electrocatalysts for overall and hybrid water splitting. *Chem. Rev.* **2024**, *124*, 3694–3812.

[4] Xu, Y. Q.; Zhang, Q.; Wang, N. N.; Huang, L. J.; Zhang, X.; Lin, H. J.; Xu, Y. C.; Chen, J. R.; Jiao, Y. Quasi-FeCo-MOF/CoS amorphous

nanosheets: A stable and highly active catalyst for electrocatalytic water splitting and monosaccharide oxidation. *Chem. Eng. J.* **2024**, *497*, 154837.

[5] Ding, X. Y.; Liu, D.; Zhao, P. J.; Chen, X.; Wang, H. X.; Oropeza, F. E.; Gorni, G.; Barawi, M.; García-Tecedor, M.; de la Peña O'Shea, V. A. et al. Dynamic restructuring of nickel sulfides for electrocatalytic hydrogen evolution reaction. *Nat. Commun.* **2024**, *15*, 5336.

[6] Meng, Y.; Zeng, P.; Yang, X. Y.; Liu, Z.; Li, X. Y.; Ye, C. F.; Li, Y.; Liu, J. P.; Su, B. L.; Chen, L. H. et al. Simultaneously achieving enhanced water adsorption and rapid adsorbed hydroxyl transfer toward MXene-based materials for highly efficient alkaline electrocatalytic hydrogen evolution. *Chem. Eng. J.* **2023**, *466*, 143372.

[7] Qin, Y. L.; Chen, Y. Z.; Zeng, X. Z.; Liu, Y. C.; Lin, X. L.; Zhang, W. L.; Qiu, X. Q. $MoNi_4$-NiO heterojunction encapsulated in lignin-derived carbon for efficient hydrogen evolution reaction. *Green Energy Environ.* **2023**, *8*, 1728–1736.

[8] Liu, X. J.; Zhao, X. M.; Cao, S. Y.; Xu, M. Y.; Wang, Y. J.; Xue, W.; Li, J. D. Local hydroxyl enhancement design of NiFe sulfide electrocatalyst toward efficient oxygen evolution reaction. *Appl. Catal. B: Environ.* **2023**, *331*, 122715.

[9] Wang, H. Y.; Sun, H.; Cao, S. Y.; Wang, Y. J.; Du, X. H.; Li, J. D. Amorphous-crystalline interface coupling induced highly active ultrathin NiFe oxy-hydroxide design towards accelerated alkaline oxygen evolution. *J. Catal.* **2024**, *430*, 115354.

[10] Bi, Y. M.; Cai, Z.; Zhou, D. J.; Tian, Y.; Zhang, Q.; Zhang, Q.; Kuang, Y.; Li, Y. P.; Sun, X. M.; Duan, X. Understanding the incorporating effect of Co^{2+}/Co^{3+} in NiFe-layered double hydroxide for electrocatalytic oxygen evolution reaction. *J. Catal.* **2018**, *358*, 100–107.

[11] Li, Y. J.; Wang, W. Y.; Huang, B. J.; Mao, Z. F.; Wang, R.; He, B. B.; Gong, Y. S.; Wang, H. W. Abundant heterointerfaces in MOF-derived hollow CoS_2-MoS_2 nanosheet array electrocatalysts for overall water splitting. *J. Energy Chem.* **2021**, *57*, 99–108.

[12] Cao, D.; Shao, J.; Cui, Y. H.; Zhang, L. P.; Cheng, D. J. Interfacial engineering of copper–nickel selenide nanodendrites for enhanced overall water splitting in alkali condition. *Small* **2023**, *19*, 2301613.

[13] Wu, Y.; Li, F.; Chen, W. L.; Xiang, Q.; Ma, Y. L.; Zhu, H.; Tao, P.; Song, C. Y.; Shang, W.; Deng, T. et al. Coupling interface constructions of MoS_2/$Fe_5Ni_4S_8$ heterostructures for efficient electrochemical water splitting. *Adv. Mater.* **2018**, *30*, 1803151.

[14] Bose, R.; Jothi, V. R.; Karuppasamy, K.; Alfantazi, A.; Yi, S. C. High performance multicomponent bifunctional catalysts for overall water splitting. *J. Mater. Chem. A* **2020**, *8*, 13795–13805.

[15] Zheng, M. Y.; Guo, K. L.; Jiang, W. J.; Tang, T.; Wang, X. Y.; Zhou, P. P.; Du, J.; Zhao, Y. Q.; Xu, C. L.; Hu, J. S. When MoS_2 meets FeOOH: A "one-stone-two-birds" heterostructure as a bifunctional electrocatalyst for efficient alkaline water splitting. *Appl. Catal. B: Environ.* **2019**, *244*, 1004–1012.

[16] Lin, J. H.; Wang, P. C.; Wang, H. H.; Li, C.; Si, X. Q.; Qi, J. L.; Cao, J.; Zhong, Z. X.; Fei, W. D.; Feng, J. C. Defect-rich heterogeneous MoS_2/NiS_2 nanosheets electrocatalysts for efficient overall water splitting. *Adv. Sci.* **2019**, *6*, 1900246.

[17] Xu, Q. C.; Jiang, H.; Zhang, H. X.; Hu, Y. J.; Li, C. Z. Heterogeneous interface engineered atomic configuration on ultrathin $Ni(OH)_2$/Ni_3S_2 nanoforests for efficient water splitting. *Appl. Catal. B: Environ.* **2019**, *242*, 60–66.

[18] Wang, K.; Huang, D. W.; Li, X. W.; Feng, K.; Shao, M.; Yi, J. B.; He, W. D.; Qiao, L. Unconventional strategies to break through the efficiency of light-driven water splitting: A review. *Electron* **2023**, *1*, e4.

[19] Huang, G.; Huang, Y. J.; Ali, A.; Chen, Z. J.; Shen, P. K.; Ni, B. J.; Zhu, J. L. Phase-controllable cobalt phosphide heterostructure for efficient electrocatalytic hydrogen evolution in water and seawater. *Electron* **2024**, *2*, e58.

[20] Mo, W. W.; Foo, J. J.; Ong, W. J. Allying interfacial engineering of 2D carbon nanosheet-, graphene-, and graphdiyne-based heterostructured electrocatalysts toward hydrogen evolution and overall water splitting. *Electron* **2024**, *2*, e20.

[21] Li, Z. C.; Pei, Y.; Ma, R. G.; Wang, Y. D.; Zhu, Y. F.; Yang, M. H.; Wang, J. C. A phosphate semiconductor-induced built-in electric field boosts electron enrichment for electrocatalytic hydrogen evolution in alkaline conditions. *J. Mater. Chem. A* **2021**, *9*, 13109–13114.

[22] Chen, L. H. K.; Xu, Q. C.; Oener, S. Z.; Fabrizio, K.; Boettcher, S. W. Design principles for water dissociation catalysts in high-performance bipolar membranes. *Nat. Commun.* **2022**, *13*, 3846.

[23] Zhao, P. D.; Peng, C.; Luo, Y. C.; Cheng, L. L.; Li, Z.; Jiao, Z. Modulating positive charge sites generations and iron oxidation state transitions in FeP_4/CoP/C p–n heterojunction toward efficient oxygen evolution. *Chem. Eng. J.* **2024**, *483*, 149121.

[24] Chen, X. H.; Fu, H. C.; Li, X. L.; Li, T.; Zhang, Q.; Li, Z. Q.; Luo, Y. H.; Lei, J. L.; Li, N. B.; Luo, H. Q. Modulating the interfacial built-in electric field in oxygen vacancies-enriched Ru/M_xO_y@C (M = V, Nb, Ta) ordered macroporous heterojunctions for electrocatalytic hydrogen production. *Chem. Eng. J.* **2023**, *467*, 143374.

[25] Zhang, X. C.; Xue, H.; Sun, J.; Guo, N. K.; Song, T. S.; Sun, J. W.; Hao, Y. R.; Wang, Q. Synergy of phosphorus vacancies and build-in electric field into NiCo/NiCoP Mott–Schottky integrated electrode for enhanced water splitting performance. *Chin. Chem. Lett.* **2024**, *35*, 108519.

[26] Xiao, Z. H.; Huang, Y. C.; Dong, C. L.; Xie, C.; Liu, Z. J.; Du, S. Q.; Chen, W.; Yan, D. F.; Tao, L.; Shu, Z. W. et al. Identification of the dynamic behavior of oxygen vacancy-rich Co_3O_4 for oxygen evolution reaction. *J. Am. Chem. Soc.* **2020**, *142*, 12087–12095.

[27] Tan, Y.; Zhu, Y. C.; Cao, X. F.; Liu, Y. H.; Li, J. Y.; Chen, Z.; Hu, J. Discovery of hydrogen spillover-based binary electrocatalysts for hydrogen evolution: From theory to experiment. *ACS Catal.* **2022**, *12*, 11821–11829.

[28] Li, J. Y.; Hu, J.; Zhang, M. K.; Gou, W. Y.; Zhang, S.; Chen, Z.; Qu, Y. Q.; Ma, Y. Y. A fundamental viewpoint on the hydrogen spillover phenomenon of electrocatalytic hydrogen evolution. *Nat. Commun.* **2021**, *12*, 3502.

[29] Gusain, M.; Dubey, A.; Das, M.; Singh, S. K. Facial surfactant-free hydrothermal synthesis of MoS_2 microflower and its effect in electrochemical properties. *J. Solid State Chem.* **2019**, *274*, 58–63.

[30] Yang, Y.; Su, R.; Wang, D. R.; Zhang, H. N.; Shang, C. L.; Wang, S.; Li, H. Additive manufactured carbon–metal phosphide electrodes for highly efficient overall water splitting. *Renewables* **2024**, *2*, 250–263.

[31] Kresse, G.; Furthmüller, J. Efficiency of *ab-initio* total energy calculations for metals and semiconductors using a plane-wave basis set. *Comput. Mater. Sci.* **1996**, *6*, 15–50.

[32] Perdew, J. P.; Burke, K.; Ernzerhof, M. Generalized gradient approximation made simple. *Phys. Rev. Lett.* **1996**, *77*, 3865–3868.

[33] Grimme, S. Semiempirical GGA-type density functional constructed with a long-range dispersion correction. *J. Comput. Chem.* **2006**, *27*, 1787–1799.

[34] Henkelman, G.; Uberuaga, B. P.; Jónsson, H. A climbing image nudged elastic band method for finding saddle points and minimum energy paths. *J. Chem. Phys.* **2000**, *113*, 9901–9904.

[35] Xu, Y. L.; Yan, M. F.; Liu, Z.; Wang, J. Y.; Zhai, Z. Z.; Ren, B.; Dong, X. X.; Miao, J. F.; Liu, Z. F. Nanostructures Ni_2P/MoP@N-doping porous carbon for efficient hydrogen evolution over a broad pH range. *Electrochim. Acta* **2020**, *363*, 137151.

[36] Song, Y.; Wu, Y. J.; Wang, Y. T.; Jia, Y. D.; Gou, H. Y.; Zhang, C. W.; Wang, G. K.; Yin, F. X. "Graphene bubble bridging" enabled flexible multifunctional carbon fiber membrane toward K^+ storage devices. *Adv. Funct. Mater.* **2024**, *34*, 2311458.

[37] Yu, H. X.; Pan, J. N.; Zhang, Y. X.; Wang, L. L.; Ji, H. C.; Xu, K. Y.; Zhi, T.; Zhuang, Z. C. Designing multi-heterogeneous interfaces of Ni-MoS_2@NiS_2@Ni_3S_2 hybrid for hydrogen evolution. *Nano Res.* **2024**, *17*, 4782–4789.

[38] Huang, L. B.; Zhao, L.; Zhang, Y.; Chen, Y. Y.; Zhang, Q. H.; Luo,

H.; Zhang, X.; Tang, T.; Gu, L.; Hu, J. S. Self-limited on-site conversion of MoO_3 nanodots into vertically aligned ultrasmall monolayer MoS_2 for efficient hydrogen evolution. *Adv. Energy Mater.* **2018**, *8*, 1800734.

[39] Xie, J. F.; Zhang, J. J.; Li, S.; Grote, F.; Zhang, X. D.; Zhang, H.; Wang, R. X.; Lei, Y.; Pan, B. C.; Xie, Y. Controllable disorder engineering in oxygen-incorporated MoS_2 ultrathin nanosheets for efficient hydrogen evolution. *J. Am. Chem. Soc.* **2013**, *135*, 17881–17888.

[40] Zhang, H. N.; Sun, Y. H.; Wang, S.; Wang, Q. Y.; Shang, Y. X.; Lee, S.; Zhang, L. Q.; Deng, L.; Yang, Y. Synergistic Ru–Co atomic pair with enhanced activity toward levulinic acid hydrogenation. *J. Colloid Interface Sci.* **2025**, *681*, 281–291.

[41] Yang, Y.; Ding, Z.; Ren, D.; Shang, C.; Li, C.; Yang, F.; Zhou, B.; Hao, S.; Sun, K.; Lee, S. Dense Ru single-atoms integrated with sulfoacids for cellulose valorization to isosorbide. *Mater. Today Sustain.* **2023**, *24*, 100494.

[42] Cheng, A.; Zhang, H. Y.; Zhong, W. H.; Li, Z. P.; Cheng, D. J.; Lin, Y. X.; Tang, Y. D.; Shao, H. Y.; Li, Z. H. Few-layer MoS_2 embedded in N-doped carbon fibers with interconnected macropores for ultrafast sodium storage. *Carbon* **2020**, *168*, 691–700.

[43] Zhang, L. Y.; Xu, Q. C.; Zhao, R. K.; Hu, Y. J.; Jiang, H.; Li, C. Z. Fe-doped and sulfur-enriched Ni_3S_2 nanowires with enhanced reaction kinetics for boosting water oxidation. *Green Chem. Eng.* **2022**, *3*, 367–373.

[44] Gao, Y.; Zhang, D. N.; Li, J. J.; Gong, H.; Jiang, C.; Xue, H. R.; Huang, X. L.; Wang, T.; He, J. P. The core/shell structure P doped MoS_2@Ni_3S_2 nanorods array for high current density hydrogen evolution in alkaline and acidic electrolyte. *Chem.—Eur. J.* **2022**, *28*, e202202410.

[45] Li, X. L.; Chen, M. C.; Ye, Y. T.; Chen, C. J.; Li, Z. L.; Zhou, Y. F.; Chen, J.; Xie, F. Y.; Jin, Y. S.; Wang, N. et al. Electronic structure modulation of nickel sites by cationic heterostructures to optimize ethanol electrooxidation activity in alkaline solution. *Small* **2023**, *19*, 2207086.

[46] Fu, G. L.; Li, W. W.; Zhang, J. Y.; Li, M. S.; Li, C. J.; Li, N.; He, Q.; Xi, S. B.; Qi, D. C.; MacManus-Driscoll, J. L. et al. Facilitating the deprotonation of OH to O through Fe^{4+}-induced states in perovskite $LaNiO_3$ enables a fast oxygen evolution reaction. *Small* **2021**, *17*, 2006930.

[47] Li, Y.; Patel, D. M.; Tsang, C. S.; Zhang, R. Q.; Liu, M. J.; Hwang, G. S.; Lee, L. Y. S. Facilitated water adsorption and dissociation on Ni/Ni_3S_2 nanoparticles embedded in porous S-doped carbon nanosheet arrays for enhanced hydrogen evolution. *Adv. Mater. Interfaces* **2021**, *8*, 2001665.

[48] Song, H. R.; Wang, J. S.; Zhang, Z. F.; Shai, X. X.; Guo, Y. Z. Synergistic balancing hydrogen and hydroxyl adsorption/desorption of nickel sulfide via cation and anion dual-doping for boosting alkaline hydrogen evolution. *Chem. Eng. J.* **2021**, *420*, 129842.

[49] Huang, T. X.; Cong, X.; Wu, S. S.; Wu, J. B.; Bao, Y. F.; Cao, M. F.; Wu, L. W.; Lin, M. L.; Wang, X.; Tan, P. H. et al. Visualizing the structural evolution of individual active sites in MoS_2 during electrocatalytic hydrogen evolution reaction. *Nat. Catal.* **2024**, *7*, 646–654.

[50] Miao, Y. Y.; Yuan, S. F.; Ren, H.; Addad, A.; Barras, A.; Roussel, P.; Amin, M. A.; Szunerits, S.; Boukherroub, R. Interface engineering of an ultrathin hierarchical phosphorus-doped MoS_2/Ni_3S_2 heterostructure on nickel foam for efficient water splitting. *ACS Appl. Energy Mater.* **2023**, *6*, 5856–5867.

[51] Fu, W. B.; Zhao, Y. Y.; Mei, J. F.; Wang, F. J.; Han, W. H.; Wang, F. C.; Xie, E. Q. Honeycomb-like Ni_3S_2 nanosheet arrays for high-performance hybrid supercapacitors. *Electrochim. Acta* **2018**, *283*, 737–743.

[52] Tang, C.; Zhong, L.; Zhang, B. S.; Wang, H. F.; Zhang, Q. 3D mesoporous van der Waals heterostructures for trifunctional energy electrocatalysis. *Adv. Mater.* **2018**, *30*, 1705110.

[53] Xiao, W.; Liu, P. T.; Zhang, J. Y.; Song, W. D.; Feng, Y. P.; Gao, D. Q.; Ding, J. Dual-functional N dopants in edges and basal plane of MoS_2 nanosheets toward efficient and durable hydrogen evolution. *Adv. Energy Mater.* **2017**, *7*, 1602086.

[54] Guo, Z. C.; Li, Y. N.; Tian, Y.; Wang, C. Ni/Ni_4N nanoparticles anchored on 3D necklace-like carbon framework as free-standing bifunctional host for practical Li-S full cells. *Chem. Eng. J.* **2024**, *496*, 154071.

[55] Wu, T.; Xu, S. M.; Zhang, Z.; Luo, M. J.; Wang, R. Q.; Tang, Y. F.; Wang, J. C.; Huang, F. Q. Bimetal modulation stabilizing a metallic heterostructure for efficient overall water splitting at large current density. *Adv. Sci.* **2022**, *9*, 2202750.

[56] Jiang, X. L.; Jang, H.; Liu, S. G.; Li, Z. J.; Kim, M. G.; Li, C.; Qin, Q.; Liu, X. E.; Cho, J. The heterostructure of Ru_2P/WO_3/NPC synergistically promotes H_2O dissociation for improved hydrogen evolution. *Angew. Chem., Int. Ed.* **2020**, *60*, 4110–4116.

[57] Zheng, X. R.; Cao, Y. H.; Wu, Z.; Ding, W. L.; Xue, T.; Wang, J. J.; Chen, Z. L.; Han, X. P.; Deng, Y. D.; Hu, W. B. Rational design and spontaneous sulfurization of NiCo-(oxy)hydroxysulfides nanosheets with modulated local electronic configuration for enhancing oxygen electrocatalysis. *Adv. Energy Mater.* **2022**, *12*, 2103275.

[58] Wang, D. R.; Luo, X. R.; Shang, Y. X.; Wang, Y. Y.; Zhang, H. N.; Wang, S.; Cui, C. M.; Lee, S.; Hao, S. J.; Yang, Y. Ultra-stable trimetallic phosphide heterostructure with regulated electronic structure for overall water splitting at high current densities. *J. Power Sources* **2024**, *614*, 234986.

[59] Yang, Y.; Wang, D. R.; Gu, L.; Luo, X. R.; Zhang, S. Y.; Ren, Y.; Liu, Q. Lattice-strained and ultra stable non-noble metal electrocatalysts for overall water splitting. *Electrochim. Acta* **2023**, *468*, 143124.

[60] Zhai, L. L.; She, X. J.; Zhuang, L. C.; Li, Y. Y.; Ding, R.; Guo, X. Y.; Zhang, Y. Q.; Zhu, Y.; Xu, K.; Fan, H. J. et al. Modulating built-in electric field via variable oxygen affinity for robust hydrogen evolution reaction in neutral media. *Angew. Chem., Int. Ed.* **2022**, *61*, e202116057.

[61] Yang, X. Y.; Yang, X. L.; Peng, Y. H.; Li, Z.; Yu, J. Q.; Zhang, Y. Regulating the built-in electric field of BiOBr by a piezoelectric mineral tourmaline and the enhanced photocatalytic property. *Ind. Eng. Chem. Res.* **2022**, *61*, 1704–1714.

[62] Chen, W. X.; Wei, W.; Li, F.; Wang, Y. J.; Liu, M.; Dong, S.; Cui, J. H.; Zhang, Y. Y.; Wang, R.; Ostrikov, K. et al. Tunable built-in electric field in Ru nanoclusters-based electrocatalyst boosts water splitting and simulated seawater electrolysis. *Adv. Funct. Mater.* **2024**, *34*, 2310690.

[63] Xu, W. X.; Wei, Y.; Zhou, S. B.; Sun, R.; Huang, X.; Han, S.; Wang, S. Z.; Jiang, J. B. Structural design strategy improving catalytic activity of binary metal sulfides interface for efficient water splitting electrocatalysts. *Electrochim. Acta* **2023**, *454*, 142377.

[64] Zhang, H.; Xi, B. J.; Gu, Y.; Chen, W. H.; Xiong, S. L. Interface engineering and heterometal doping Mo-NiS/$Ni(OH)_2$ for overall water splitting. *Nano Res.* **2021**, *14*, 3466–3473.

[65] Liu, H. B.; Gao, J.; Xu, X. C.; Jia, Q. H.; Yang, L.; Wang, S. T.; Cao, D. P. Oriented construction Cu_3P and Ni_3P heterojunction to boost overall water splitting. *Chem. Eng. J.* **2022**, *448*, 137706.

[66] Zhang, W.; Yan, H. J.; Liu, Y.; Wang, D. X.; Jiao, Y. Q.; Wu, A. P.; Wang, X. W.; Wang, R. H.; Tian, C. G. Multi-interfacial engineering of an interlinked Ni_2P-MoP heterojunction to modulate the electronic structure for efficient overall water splitting. *J. Mater. Chem. A* **2023**, *11*, 15033–15043.

[67] Deng, R. X.; Yao, H. Q.; Wang, Y. X.; Wang, C. N.; Zhang, S. Q.; Guo, S. S.; Li, Y. L.; Ma, S. L. Interface effect of Fe doped NiSe/Ni_3Se_2 heterojunction as highly efficient electrocatalysts for overall water splitting. *Chem. Eng. J.* **2024**, *488*, 150996.

[68] Tian, G. L.; Liu, X. L.; Song, S. H.; Zhang, Q. Q.; Wang, Z. Y.; Liu, Y. Y.; Zheng, Z. K.; Cheng, H. F.; Dai, Y.; Huang, B. B. et al. *In situ*

formation of CoP/Co_3O_4 heterojunction for efficient overall water splitting. *Chem.—Eur. J.* **2023**, *29*, e202301478.
[69] Xiao, Y. X.; He, Z. Z.; Bai, L. C.; Chen, Q.; Ying, J. Fe-doped Ni_3S_2/Ni_xP heterojunction with enhanced electron transfer for efficient electrochemical water splitting. *J. Phys. Chem. C* **2023**, *127*, 24583–24590.
[70] Li, D.; Zhou, C. J.; Yang, R.; Xing, Y. Y.; Xu, S. J.; Jiang, D. L.; Tian, D.; Shi, W. D. Interfacial engineering of the Co_xP-Fe_2P heterostructure for efficient and robust electrochemical overall water splitting. *ACS Sustainable Chem. Eng.* **2021**, *9*, 7737–7748.
[71] Li, X. T.; Liu, Y. Z.; Sun, Q. D.; Huang, W. H.; Wang, Z. L.; Chueh, C. C.; Chen, C. L.; Zhu, Z. L. Surface engineered CoP/Co_3O_4 heterojunction for high-performance bi-functional water splitting electro-catalysis. *Nanoscale* **2021**, *13*, 20281–20288.
[72] Xiao, Y. H.; Shen, Y.; Su, D. C.; Zhang, S. W.; Yang, J. L.; Yan, D. F.; Fang, S. M.; Wang, X. Z. Engineering $Cu_{1.96}S$/Co_9S_8 with sulfur vacancy and heterostructure as an efficient bifunctional electrocatalyst for water splitting. *J. Mater. Sci. Technol.* **2023**, *154*, 1–8.
[73] Wu, Y. S.; Xie, Y. F.; Niu, S. W.; Zang, Y. P.; Cai, J. Y.; Bian, Z. N.; Yin, X. W.; Fang, Y. Y.; Sun, D.; Niu, D. et al. Accelerating water dissociation kinetics of Ni_3N by tuning interfacial orbital coupling. *Nano Res.* **2021**, *14*, 3458–3465.
[74] Liu, X.; Ni, K.; Niu, C. J.; Guo, R. T.; Xi, W.; Wang, Z. Y.; Meng, J. S.; Li, J. T.; Zhu, Y. W.; Wu, P. J. et al. Upraising the O 2p orbital by integrating Ni with MoO_2 for accelerating hydrogen evolution kinetics. *ACS Catal.* **2019**, *9*, 2275–2285.
[75] Sun, Y. Q.; Bao, Y. W.; Bu, X. M.; Yue, K. H.; Zhang, H.; Zhang, Y. X.; Yin, D.; Yang, S. W.; Ho, J. C.; Wang, X. Y. Solid redox equilibrium via d-band centers regulation in the MoS_2/Ni_3S_2 heterojunction for efficient selective oxidation of 5-hydroxymethylfurfural. *Mater. Today Energy* **2024**, *39*, 101463.
[76] Aftab, J.; Ali, A.; Mehmood, S.; Aftab, A.; Ahmad, I.; Bhopal, M. F.; Hussain, M.; Shah, Z. U.; Shah, A. U.; Padhiar, M. A. et al. Facile synthesis of synergetic MoO_2/MoS_2@GO nanohybrid as energy-efficient electrode material for high-performance asymmetric supercapacitor applications. *J. Energy Storage* **2023**, *74*, 109324.
[77] Man, H.; Feng, J. J.; Wang, S. F.; Li, S. Y.; Li, P.; He, H. W.; Raróg-Pilecka, W.; Zhao, J.; Zhang, J. H.; Fang, F. et al. Ultra-fast surface reconstruction enabled by the built-in electric field in heterostructured CoS_2/CuS for water electrolysis. *Cell Rep. Phys. Sci.* **2022**, *3*, 101059.
[78] Li, D. R.; Wan, W. J.; Wang, Z. W.; Wu, H. Y.; Wu, S. X.; Jiang, T.; Cai, G. X.; Jiang, C. Z.; Ren, F. Self-derivation and surface reconstruction of Fe-doped Ni_3S_2 electrode realizing high-efficient and stable overall water and urea electrolysis. *Adv. Energy Mater.* **2022**, *12*, 2201913.
[79] Lin, M.; Gu, M. Z.; Deng, X. Y.; Xie, Q.; Zhang, X. J. Interface engineered Ni_3Se_2/Ni_3S_2/NF heterostructure as a highly efficient electrocatalyst for robust oxygen evolution reaction. *Chem. Eng. J.* **2023**, *468*, 143705.
[80] Zhao, X.; Liu, M. J.; Wang, Y. C.; Xiong, Y.; Yang, P. Y.; Qin, J. Q.; Xiong, X.; Lei, Y. P. Designing a built-in electric field for efficient energy electrocatalysis. *ACS Nano* **2022**, *16*, 19959–19979.
[81] Zhang, S. C.; Tan, C. H.; Yan, R. P.; Zou, X. F.; Hu, F. L.; Mi, Y.; Yan, C.; Zhao, S. L. Constructing built-in electric field in heterogeneous nanowire arrays for efficient overall water electrolysis. *Angew. Chem., Int. Ed.* **2023**, *62*, e202302795.
[82] Chen, T.; Li, B.; Song, K.; Wang, C. X.; Ding, J. W.; Liu, E. Z.; Chen, B.; He, F. Defect-activated surface reconstruction: Mechanism for triggering the oxygen evolution reaction activity of NiFe phosphide. *J. Mater. Chem. A* **2022**, *10*, 22750–22759.
[83] Wan, K.; Luo, J. S.; Zhou, C.; Zhang, T.; Arbiol, J.; Lu, X. H.; Mao, B. W.; Zhang, X.; Fransaer, J. Hierarchical porous Ni_3S_4 with enriched high-valence Ni sites as a robust electrocatalyst for efficient oxygen evolution reaction. *Adv. Funct. Mater.* **2019**, *29*, 1900315.